
Article:
Saeed, H.K., Sreedharan, S. and Thomas, J.A. orcid.org/0000-0002-8662-7917 (2020) Photoactive metal complexes that bind DNA and other biomolecules as cell probes, therapeutics, and theranostics. Chemical Communications, 56 (10). pp. 1464-1480. ISSN 1359-7345

https://doi.org/10.1039/c9cc09312e

Journal Name

Dynamic Article Links ►

Cite this: DOI: 10.1039/c0xx00000x

www.rsc.org/xxxxxx

ARTICLE TYPE

Photoactive Metal Complexes That Bind DNA and Other Biomolecules as Cell Probes, Therapeutics, and Theranostics

Hiwa K Saeed,[a] Sreejesh Sreedharan,[b] and Jim A Thomas[c]*

Received (in XXX, XXX) Xth XXXXXXXXX 20XX, Accepted Xth XXXXXXXXX 20XX

DOI: 10.1039/b000000x

This review discusses the advantages of using luminescent d^6-transition-metal complexes as cell probes for optical microscopy. In particular it focusses on the Thomas group's use of specific complexes as "building blocks" toward the construction of biomolecular binding substrates, with DNA being a particular target. Using this approach, a range of new imaging probes for conventional optical microscopy, nanoscopy and transmission electron microscopy have been identified. Through selection of specific metal centres and by substitution of coordinated ligands we illustrate how new chemotherapeutics, photo-therapeutics, and theranostics have been identified and developed from the original architectures.

Introduction

Barnet Rosenberg's discovery that cisplatin, a simple coordination complex first described in 1845, possessed potent chemotherapeutic action was a revelation.[1] By the 1980s cisplatin was in clinical use as an antineoplastic drug throughout the world and two other derivatives eventually gained global approval. [2,3] Consequent studies revealed that these compounds derive their therapeutic action through irreversibly binding to nuclear DNA. [4-6] Even today, platins are used to treat a wide-range of cancers with around half of all chemotherapy schedules including a platin. [7,8]

In their original report on the anti-tumour properties of cisplatin, Rosenburg and colleagues observed that; "*at present, inorganic chemistry is largely unexplored for this property*." [1] Yet - despite this observation and the success of the platins – research into the biological activity of other platinum group metals was still slow to develop.

It was not until the Barton group's trail-blazing work from the 1980s onward[9-11] that ruthenium began to attract sustained attention. After demonstrating that polypyridyl ruthenium complexes could interact reversibly with DNA, the group identified the striking properties of $[Ru(bpy)_2dppz]^{2+}$ (where bpy = 2,2'-bipyridine, dppz = dipyrido[3,2-a:2',3'-c]phenazine), which became known as the "DNA light-switch". [12] This complex is non-emissive in protic solvents, with the expected Ru→dppz-based metal-to-ligand charge-transfer, ^{3}MLCT, emission being non-radiatively quenched by hydrogen bonding interactions with solvent molecules. [13] On the addition of B-DNA the extended dppz ligand intercalates into the duplex and the emission from the complex is "switched on" as its solvent accessibility is greatly reduced. Subsequent work on this complex, and its 1,10-phenanthroline (phen) derivative, revealed that chirality played a part in this recognition process.

Hiort, *et al*, were the first to separate the two enantiomers of $[Ru(phen)_2dppz]^{2+}$ and show that, while there is not a large difference in their DNA binding affinity, the quantum yield for DNA-bound Δ-$[Ru(phen)_2dppz]^{2+}$ is around an order of magnitude larger than its Λ-analogue. Intriguingly, they also found that both bound enantiomers display two emission lifetimes. It was postulated that these effects were due to differences in binding geometries. [14] Recently, a series of definitive X-ray studies from Cardin and co-workers have cast light onto this hypothesis.

Duplex bound structures exclusively containing Δ-$[Ru(phen)_2dppz]^{2+}$ and Λ-$[Ru(phen)_2dppz]^{2+}$. or a mixture of both enantiomers, have been reported and - although the bound enantiomers do show a variety of motifs – those involving the Δ-form display the greatest "solvent shielding" of the dppz ligand.[15-17]

Despite these exciting properties - seen from the perspective of developing biological probes or therapeutic leads - the original DNA light-switch system is not perfect. Drawbacks include the low selectivity of the light-switch effect. In terms of sequence effect with duplex DNA, binding to AT sequences produce a red shift in emission of ~15 nm compared to GC analogues and there is evidence of a binding preference for extended AT sequences. [18] In terms of structure, although binding to A-DNA and folded RNA only induces an insubstantial increase in luminescence, a light-switch effect still occurs on binding to single-, triple- and quadruple-stranded DNA as well as Z-form duplex and the interpenetrated i-motif[18-21] Furthermore, a similar emission enhancement is observed on binding to micelles, [22] and even pathogenic peptide and protein aggregates. [23,24] More importantly, the take up of these complexes by live cells is generally poor. Even though lipophilic derivatives passively diffuse into cells, they preferentially localize within the cytoplasm[25] and localization

within the nucleus can only be accomplished by covalent attachment to nuclear targeting moieties. [26,27]

With an original aim of amplifying chiral effects in DNA recognition, Nordén, Lincoln, and co-workers synthesized a series of dinuclear complexes containing linked $[Ru(LL)_2dppz]^{2+}$ units (LL = bpy or phen). [28-31] Studies over the last two decades have illustrated the fascinating properties of these architectures. As the two $Ru^{II}(LL)_2$ units are tethered together at the dppz moiety these complexes can only intercalate into DNA through a threading interaction. This means they display very high binding affinities and extremely slow dissociation kinetics. The nature of this threading interaction is also affected by how closely the two $Ru^{II}(LL)_2$ are tethered together. Longer linkers allow each $[Ru(LL)_2dppz]^{2+}$ centre to insert into a separate site resulting in bis-intercalation, [29,32] but directly linked $[Ru^{II}(LL)_2dppz]$ centres act as a single unit and mono-intercalate. [33] As a result, like their mononuclear analogues, the stereoisomers of threaded bis-intercalators display little difference in binding parameters and preferences, whereas the threaded mono-intercalators show a kinetic binding preference for AT-rich sequences, an effect which is further amplified by chirality as selectivity is particularly pronounced for the ΔΔ form of the bpy complex. [34,35]

Complexes that display the light-switch effect have an obvious application in microscopy. Optical microscopy is a vital technique for research in wide range of fields including cytology, molecular biology, medicine, and diagnostics. In this context, emission-based microscopes using luminescent dyes provide optimal contrast, thus providing high sensitivity and image resolution. Consequently, driven by the need to image individual cell components, the identification of luminescent probes that bind to intracellular targets with high specificity has become an important aim of research.[36]

Recent work has also demonstrated that d^8-metal complexes are well-suited to for this form of microscopy. For example, the excited state of complexes like the DNA light-switch complex are emissive from triplet states (formally phosphorescence) and thus have large Stokes shifts and long-lived luminescence.[36-38] Through their octahedral coordination geometry they also provide a 3-D "scaffold" to arrange ancillary ligands into recognition motifs.[39,40] Therefore, the Thomas group has been looking at develop systems that could incorporate some of the attractive properties displayed by the oligonuclear complexes described above.

A modular approach to bis-intercalators

Inspired by the research described in the previous section, the Thomas group first set out to develop a more modular approach toward the construction of dinuclear complexes based on the Ru^{II}(dppz) intercalative platform. A two-step method involving the coordination of a bridging ligand to suitable mononuclear "building blocks" was identified – Scheme 1.

Complexes with facially coordinated ligands were deliberately chosen for two reasons. First, it simplifies the synthesis of oligomeric structure as it leads to achiral geometries, removing the need to separate stereoisomers, often a laborious task – although chirality can be consequently added selectively using specific ligands. Second, linking of such units by a suitable bridging ligand "tether" results in a dinuclear complex with co-planar intercalation sites.

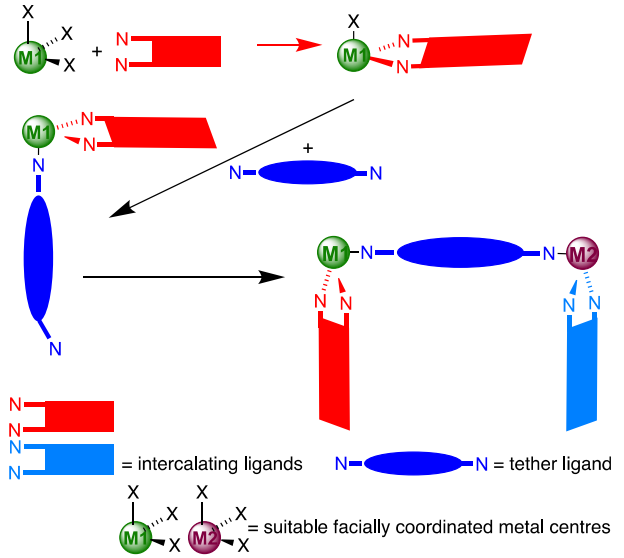

Scheme 1. Generalised synthetic route to the construction of structural complex bis-intercalating systems based on M(dppz) centres and analogues.

Identifying suitable building blocks

One suitable starting point already existed; during 1995 the Schanze and Yam groups both reported on the DNA binding properties of $[Re(CO)_3(L)dppz]^+$ (L = pyridine or 4-picoline), synthesized from $[ReCl(CO)_5]$. [41,42] This complex does not display a true light-switch effect as it only show a ×13 enhancement in emission and, because it is a monocation, it binds DNA with an order of magnitude lower affinity. Nevertheless, it is of great interest as its excited state is strongly photo-oxidizing and so it is capable of generating DNA damage on intercalation. [43]

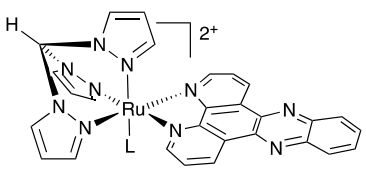

$\mathbf{1}^{2+}$: L = MeCN; $\mathbf{2}^{2+}$: L = pyridine

Fig. 1 structure of $\mathbf{1}^{2+}$ and $\mathbf{2}^{2+}$

The first new synthetic target was a suitable Ru^{II}(dppz) building block. This was obtained by adapting a method the Meyer group used to create a series of complexes such as $[RuCl(tpm)(phen)]^+$ (where tpm = tris(pyrazolyl)methane).[44] Using $[RuCl(tpm)(dppz)]^+$ as a "building block" we initially synthesized mononuclear dications $\mathbf{1}^{2+}$ and $\mathbf{2}^{2+}$ - Fig. 1. Studies revealed that, like the parent complex, $\mathbf{1}^{2+}$ and $\mathbf{2}^{2+}$ display a full light-switch effect and bind to CT-DNA with comparable affinities. Yet, further experiments showed that the binding selectivity of $\mathbf{1}^{2+}$ differs to that of $[Ru(LL)_2dppz]^{2+}$.

Previous photophysical and biophysical experiments indicated that the parent $[Ru(bpy)_2dppz]^{2+}$ complex displays a preference for AT tracks. For example, the wavelength of its emission on binding to mixed sequences is close to that observed when it is bound to synthetic AT oligonucleotides. Furthermore, AT-bound complexes display longer excited-state life-times (~300-800ns)

than when bound to GC sequences (~200- 400ns). Both these observations indicate the complex is more deeply intercalated into AT steps. Indeed, analysis of data obtained when Δ-$Ru(phen)_2dppz^{2+}$ was added to a 1:1 mixture of poly d(AT) and poly d(GC), indicated an ~85% binding preference for poly d(AT).

In contrast to these observations, isothermal calorimetry (ITC) studies on $\mathbf{1}^{2+}$ show that it has an order of magnitude binding preference for GC- over AT-sequences. Moreover, although previous ITC experiments had shown that intercalation of $Ru(phen)_2dppz^{2+}$ into duplex DNA is an endothermic, entropically driven event[46] - and an almost identical thermodynamic signature is observed when $\mathbf{1}^{2+}$ binds to poly(dA)·poly(dT) - the interaction of $\mathbf{1}^{2+}$with poly(dG)·poly(dC) shows a much lower favourable entropy change and is actually an exothermic process. This suggests that the ancillary ligands of $\mathbf{1}^{2+}$ make favourable contacts with base residues within the poly(dG)·poly(dC) duplex.

Homometallic dinuclear M(dppz) complexes

Using Scheme 1 as a starting point, we then looked at ways to connect these building blocks and began by focusing on simple homo-metallic systems. This first led to the isolation of $\mathbf{3}^{2+}$ Fig. 2, which showed interesting binding properties.

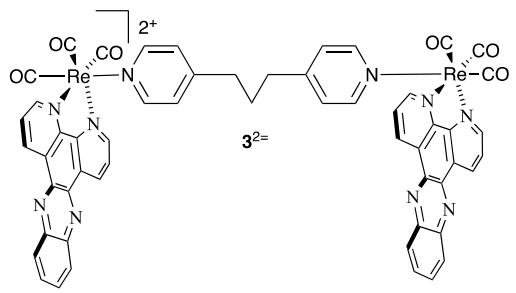

Fig 2 Structures of dinuclear Re^{I} complex $\mathbf{3}^{2+}$

Contrary to the scheme, we found that $\mathbf{3}^{2+}$ could only be isolated by linking the two Re^{I} centres together first and then coordinating the dppz ligands in a second step. [47] Although the dinuclear complex is not luminescent, bands in its absorption spectrum display hypochromic changes on addition of DNA characteristic of intercalative interactions. Titrations based on these changes revealed that the complex binds to duplex DNA in two steps.

The first phase of binding occurs up to [DNA]:[complex] mixing ratios of around 10:1; interestingly, apparent saturation for this event occurs when the percentage hypochromicity is half that observed for its mononuclear analogues. Fits of these data to the well-established McGhee-von Hippel model resulted in a slightly larger binding affinity (K_b = 7 3 x10^5 mol^{-1} dm^3) and site size (4.5 base pairs, bp, compared to 3.2 bp). When more DNA was added, further hypochromicity was observed, resulting in a much shallower binding curve that did not reach saturation, even at higher [DNA]:[complex] ratios.

These data suggest that $\mathbf{3}^{2+}$ initially mono-intercalates and its binding is enhanced compared to the mononuclear analogues by its increased cationic charge. The second event was attributed to a non-specific interaction and, as it only occurs at high DNA concentrations, it seems that this may be due to inter-strand binding.

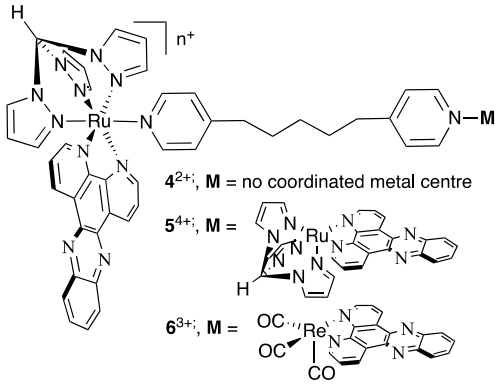

Fig 3 Mononuclear complex $\mathbf{4}^{2+}$ is an intermediate in the synthesis of dinuclear Ru^{II} complex $\mathbf{5}^{4+}$ and Heterometallic Ru^{II}/Re^{I} complex $\mathbf{6}^{3+}$

We then explored the synthesis of similar Ru^{II}(dppz) systems. In this case, to increase the likelihood of bis-intercalation into the same duplex strand, we chose to use a slightly longer linker. So, using the route outlined in Scheme 1, complex $\mathbf{4}^{2+}$ was used to synthesize $\mathbf{5}^{4+}$ - Fig 3. Unlike $\mathbf{3}^{2+}$ complexes $\mathbf{4}^{2+}$ and $\mathbf{5}^{4+}$ *do* display a light-switch effect and emission titrations with $\mathbf{5}^{4+}$ indicated it binds to DNA monophasically with an increased K_b of 2.1 x10^6 mol^{-1} dm^3. Nonetheless, this figure is still appreciably lower than those of their threading analogues. To explore these issues in more detail, we went on to investigate the binding properties of $\mathbf{5}^{4+}$ using isothermal calorimetry, ITC.

The interaction of $\mathbf{5}^{4+}$ and mononuclear $\mathbf{4}^{2+}$ with both poly(dA),poly(dT) and poly(dG),poly(dC) were compared. These studies confirmed that $\mathbf{5}^{4+}$ does bind to duplex structures in a single phase and, notably, the binding site sizes for $\mathbf{5}^{4+}$ are appreciably larger than those for $\mathbf{4}^{2+}$; for example, the calculated site sizes for the two complexes with poly(dA),poly(dT) are 7.6 bp and 3.3 bp respectively. Furthermore, although both of the complexes display endothermic, entropically-driven interactions and their binding free energy changes are similar, there are distinct differences. [48]

Whilst its selectivity is reduced compared to $\mathbf{1}^{2+}$, complex $\mathbf{4}^{2+}$ still binds to poly(dG),poly(dC) with an affinity that is approximately ×2 higher than that for poly(dA),poly(dT). Yet, within experimental error, complex $\mathbf{5}^{4+}$ shows no difference in its binding affinity for the two oligonucleotides. Strikingly, the favourable TΔS contributions for binding of $\mathbf{5}^{4+}$ to both sequences are bigger than those for the mononuclear complexes, but this is balanced by a corresponding increase in the opposing ΔH term.

A heterometallic dinuclear M(dppz) complex

Again, using complex $\mathbf{4}^{2+}$ as a building block, Scheme 1 provided a convenient route toward the first Re^{I}(dppz)/Ru^{II}(dppz) complex, $\mathbf{6}^{3+}$, in which the metal centres are linked with the same tether ligand used in $\mathbf{5}^{4+}$ - Fig 3.[49]

The inclusion of the $Re^{I}(CO)_3$(dppz) moiety within $\mathbf{6}^{3+}$ meant that its excited state dynamics could be probed by time-resolved infra-red, TRIR, spectroscopy. This technique showed that photo-excitation initially led to the population of a dppz-centered $\pi\rightarrow\pi^*$ ^{3}IL state observed in mononuclear $[Re(CO)_3(L)dppz]^+$ complexes. In the mononuclear systems, TRIR studies had shown that the ^{3}IL state then decays into a Re(dπ)→dppz(π*) MLCT manifold. In equivalent experiments with $\mathbf{6}^{3+}$ only ^{3}IL state decay was observed. Furthermore, steady-state photophysical studies on this system

showed that excitation of the Re^{I}(dppz) unit solely results in Ru^{II}(dppz)-based emission. Taken together these experiments indicate energy transfer from the Re^{I} to the Ru^{II} centre, a phenomenon that has been observed in other ligand bridged Ru^{II}-Re^{I} complexes.

As might be expected from the observations described above, on addition of CT-DNA, $\mathbf{6}^{3+}$ displays a Ru→dppz-based ^{3}MLCT light-switch effect with a lifetime that is comparable to $\mathbf{4}^{2+}$. The binding affinity of $\mathbf{6}^{3+}$, calculated from these emission changes is comparable to $\mathbf{5}^{4+}$ which is an order of magnitude higher than $[Re(CO)_3(py)dppz]^{+}$. Given that; the excited state of the latter complex can photo-damage DNA, complex $\mathbf{6}^{3+}$ displays an improved binding affinity compared to mononuclear complexes, and the irradiation of $\mathbf{6}^{3+}$ leads to the population of the dppz-centered π→π* ^{3}IL state associated with photo-oxidation, the DNA photo-nicking properties of $\mathbf{6}^{3+}$ were also investigated.

It was found that addition of $\mathbf{6}^{3+}$ to aqueous buffer solutions of pBR322 plasmid DNA followed by photo-irradiation led to the generation of relaxed singly nicked plasmid and at higher loadings of the complex complete degradation of the DNA rapidly occurred. These observations confirmed that the complex could simultaneously function as a DNA light switch *and* a photo-activated "scissors" for DNA.

Exploring steric and electronic effects in mononuclear building blocks

Despite displaying promising physical and biophysical properties, which included larger binding site sizes, the fact that the first generation of linked dinuclear complexes displayed DNA binding affinities that were comparable to their mononuclear analogues was disappointing. Simple thermodynamic considerations suggest that binding constants for bis-intercalators should be the square of their monomeric analogues. [50] As outlined above, a comparison of ITC-based DNA binding data for $\mathbf{4}^{2+}$ and $\mathbf{5}^{4+}$ showed that the dinuclear complex actually displays a larger unfavourable ΔH term compared to its mononuclear analogue, resulting in very similar binding free energies for the two complexes. This hinted that unfavourable steric interactions may have a deleterious influence on the binding of the dinuclear complex, Further evidence for this hypothesis came from experiments on derivatives of $\mathbf{2}^{2+}$ that led to very surprising observations.

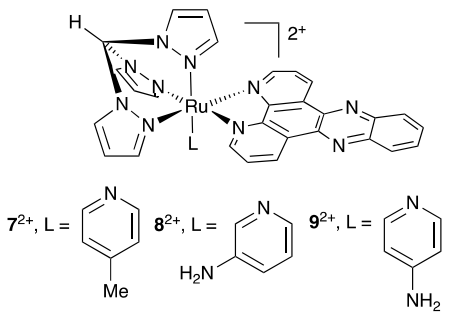

Fig 4 Mononuclear Ru^{II} complexes $\mathbf{7}^{2+}$ - $\mathbf{9}^{2+}$

When we compared $\mathbf{7}^{2+}$, $\mathbf{8}^{2+}$, and $\mathbf{9}^{2+}$, Fig. 4, we found that, as expected, $\mathbf{7}^{2+}$ and $\mathbf{8}^{2+}$ possess DNA binding properties that are very similar to $\mathbf{1}^{2+}$; for example, they show a DNA light-switch effect when binding to a duplex due to a intercalative interaction and - although the binding affinity of $\mathbf{7}^{2+}$ is slightly reduced compared to the parent complex (presumably due to the increased steric demand produced by the methyl group of the coordinated picoline ligand) - it still possesses a K_b (> 10^6 M^{-1}) that approximates that of other mononuclear Ru(dppz) systems. Unexpectedly, we found that complex $\mathbf{9}^{2+}$ displays very different binding properties.

Despite the complex still exhibiting bright ^{3}MLCT-based emission in non-aqueous solvents, in water - even in the presence of excess DNA – its light-switch remains "switched off." Titrations based on changes of its absorbance spectrum confirmed that the complex does bind DNA, but its binding affinity is an order of magnitude lower than that of $\mathbf{2}^{2+}$ and $\mathbf{8}^{2+}$. Significantly, viscosity experiments revealed that $\mathbf{9}^{2+}$ is no longer a DNA intercalator. These observations were explained through a combination of computational and NMR-based studies.

Using quantum-based, density functional theory (DFT) the structural and electronic properties of $\mathbf{2}^{2+}$, and $\mathbf{7}^{2+}$ - $\mathbf{9}^{2+}$ were compared. It was found that, in all cases, the pyridyl ligand in these complexes is held so that its plane lies parallel to the long axis of the complex and a significant activation barrier against rotation away from this conformation exists. However, significant differences between the complexes was revealed in a comparison of rotational freedom around their Py-NH_2 and Py-Me bonds, respectively. In contrast to $\mathbf{7}^{2+}$, where the Py-Me bond has a low torsional barrier for rotation, calculations on $\mathbf{9}^{2+}$ suggested that the lone pair of the amino group is not specifically located on the nitrogen and there is also a large rotational barrier around the NH_2-py bond. Both these results are indicative of a large contribution from a quinoidal structure for the coordinated ligand, as a consequence the flat NH_2 unit is held in the same plane as the pyridine ring, parallel to the long axis of the dppz ligand.

Thanks to a collaboration with Mike Williamson, an NMR-based structure of $\mathbf{2}^{2+}$ bound to the octanucleotide $d(CGAGCTCG)_2$ sequence was obtained which provided further insights into the unusual binding properties of $\mathbf{9}^{2+}$ - Fig 5.

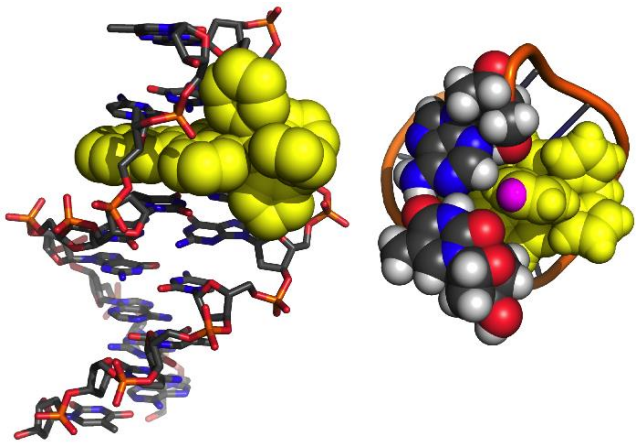

Fig. 5 Left: NMR-based structure for the major conformation of $\mathbf{2}^{2+}$ intercalated from the minor groove into the sequence $d(CGAGCTCG)_2$. Right: View from above with the final base-pair step above the intercalation site (shown in a space filling mode), revealing the close contact between this step and the 4-H of the py ligand of $\mathbf{2}^{2+}$, highlighted in cyan. Adapted from Reference 51 with permission. (Biological Magnetic Resonance Data Bank Entry 16291)

It was found that the complex intercalates from the minor groove with the dppz inserted into the G^3–A^3 step. In the main binding geometry, the axial pyridine ligand points toward the

terminal base pairs and the coordinated tpm points toward the centre of the duplex. The structural model derived from the NMR data shows that the C^1–G^8 base pair forms a ledge that protrudes exactly level with the 4-H of the py ligand of $\mathbf{1}^{2+}$, suggesting that functional groups in the 4-position of py-based ligands could indeed hinder intercalative binding by related derivatives.[51]

Taken with the DFT calculations, it seems that during intercalation the 4-methyl group of $\mathbf{7}^{2+}$ can rotate to minimize unfavourable steric interactions with closely positioned DNA residues. Contrastingly, if $\mathbf{9}^{2+}$ intercalated with a similar geometry its coordinated 4-NH_2py ligand would be held rigidly in in a sterically unfavourable position; consequently, groove binding becomes the energetically favoured binding mode. Variable temperature experiments on $\mathbf{2}^{2+}$ and $\mathbf{9}^{2+}$ revealed another facet of this fascinating phenomenon.

Temperature dependent binding modes

At first, the DNA binding thermodynamics of the two complexes at 25°C was investigated. It was found that in these conditions binding is entropically driven, but though the interaction involving $\mathbf{2}^{2+}$ is an endothermic process, there is no heat change associated with the interaction of $\mathbf{9}^{2+}$. Then similar experiments at 10°C and 35°C were carried out to obtain estimates of $\Delta C_{p.}$. The data obtained for $\mathbf{2}^{2+}$ yielded an estimated ΔC_p of -84 cal mol^{-1} K^1. This value is comparable with those of other DNA intercalators and is consistent with the release of water through a hydrophobic interaction. Unexpectedly, the temperature variance of ΔH and ΔS for $\mathbf{9}^{2+}$ was found to be much higher, leading to a large ΔC_p (-219 cal mol^{-1} K^1). This distinctive temperature response means that at 10°C the DNA binding thermodynamics for $\mathbf{9}^{2+}$ are almost identical to those for $\mathbf{2}^{2+}$, suggesting that at the lower temperature $\mathbf{9}^{2+}$ becomes an intercalator. This was confirmed by viscosity experiments and the remarkable observation that at 10°C $\mathbf{9}^{2+}$ *does* display a light-switch effect. What is more, once intercalated, the complex continues to luminesce even when the ambient temperature is raised to 25°C.[52]

As small changes in the structure of $\mathbf{2}^{2+}$ and its mononuclear derivatives produced such large differences in DNA recognition properties, we set out to explore whether similar effects modulate the binding properties of their dinuclear analogues.

Making the right links with dinuclear Ru(dppz) systems.

The fact that the photophysical and biophysical properties of $\mathbf{8}^{2+}$ are very similar to $\mathbf{2}^{2+}$ whilst $\mathbf{9}^{2+}$ are radically different was striking. This observation prompted us to synthesize a series of eight mono- and dinuclear complexes in which tethers were attached to the 3- or 4- position of the coordinated pyridyl units of the bridging ligand – Fig 6

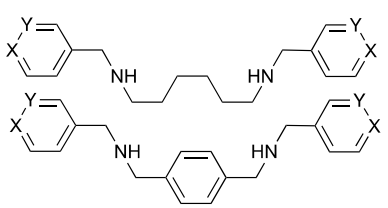

Fig. 6. Ligands used in the synthesis of a series of mono- and dinuclear Ru^{II} complexes, analogous to those shown in Fig 4, designed to investigate the effect of tethering moiety on DNA binding properties. In 4-py derivatives X = N, Y = CH; in 3-py derivatives X = CH, Y = N

The connecting tethers possessed potential DNA recognition sites in themselves and were also chosen to investigate the effects of linker rigidity on the binding properties of resultant metallo-intercalators.[53] Although simple absorption-based DNA titrations indicated that the mono- and dinuclear complexes containing the central aromatic ring in its linker bind to DNA with higher affinities, more profound differences were revealed in viscosity experiments.

All mono- and dinuclear complexes containing 4-py based ligands induced increases in the relative viscosity of aqueous DNA solutions, providing *prima facie* evidence of intercalation. The complexes containing the more flexible 4py-x-4py induced larger changes than the 4py-Y-4py-based complexes. Furthermore, unlike the mono- and dinuclear 4py-Y-4py-complexes, which both had very similar effects on viscosity; the mononuclear 4py-x-4py complex induced appreciably larger changes than its dinuclear analogue, changes that approached those caused by the archetypical intercalator ethidium bromide. In contrasts, all the complexes containing 3-py based ligands produce large increases in viscosity, comparable or greater than ethidium bromide and the dinuclear complexes induce changes that are comparable or larger than their mononuclear equivalents.

These results provided further evidence that substituents in the 4-position of the coordinating pyridyl moiety modulate the tight intrinsic binding properties of the Ru-dppz intercalative platform much more than 3-py analogues.

ITC was then used to investigate this issue in more detail. This analysis showed that three of the complexes containing 4-py based ligands showed similar thermodynamic signatures indicative of entropy-driven binding. However, one dinuclear complex, displayed a very different thermodynamic profile, with binding being enthalpy driven and entropy opposed. Within this group, the ITC-measured binding constants for the dinuclear complexes were actually lower than that for the corresponding monomeric complex and binding site size remained more or less constant.

The 3-py-linked complexes display very different binding thermodynamics. The dinuclear complexes have higher affinities for DNA than their corresponding mononuclear complexes, with affinities up to two orders of magnitude larger than ITC-based estimates obtained for $\mathbf{4}^{4+}$ and $\mathbf{5}^{2+}$. Further analysis of the data suggested that these complexes bind to DNA with mixed groove binding/intercalative interactions. Clearly, these studies confirmed that the nature of the tether ligand can greatly modulate the binding properties of our linked systems.

Heteroleptic Ru(dppz/dppn) systems.

In the course of identifying new building blocks for our oligonuclear systems, we discovered that Ru^{II}(dppn) complexes possess interesting properties that are quite different to their Ru^{II}(dppz) analogues.

In the 1990s the Barton group had reported that despite binding DNA with affinities that are comparable to DNA light-switch systems, $[Ru(bpy)_2(dppn)]^{2+}$ (dppn = benzo[*i*]dipyrido[3,2-*a*:2′,3′-*c*]phenazine) is not luminescent, even when bound.[54] Over a decade later, we found that a range of complexes containing the Ru^{II}(dppn) moiety were all virtually non-emissive in any solvent. This prompted us to investigate the excited state properties of complexes like $[Ru(bpy)_2(dppn)]^{2+}$ in more detail.

Transient absorption spectroscopy showed that all the

complexes containing the Ru^{II}(dppn) unit displayed a long-lived dppn-based ππ* triplet state, which is an efficient singlet oxygen sensitizer, producing $^1O_2$ yields of >70%.[55] This observation suggested that such complexes could be useful as sensitizers for photodynamic therapy. PDT. Later work by the Turro group confirmed this suggestion. In a detailed study they showed that photoexcitation of $[Ru(bpy)_2(dppn)]^{2+}$ results in occupation of *two* excited states: the ππ* state we described, and a strongly oxidizing ^{3}MLCT state capable of directly photo-damaging G-sites of DNA.[56] Prompted by these encouraging observations we investigated the properties of dinuclear complexes that incorporated the Ru^{II}(dppn) moiety.

By modifying Scheme 1, mononuclear complex $\mathbf{11}^{2+}$ was used to synthesize $\mathbf{12}^{4+}$ and its heteroleptic dppz/dppn analogue $\mathbf{13}^{4+}$ - Fig. 7. The properties of the three new complexes were then compared to those of their dinuclear Ru(dppz) analogue.[57] All four complexes had comparable DNA binding affinities, but their photophysical properties are strikingly different. Whereas the singlet oxygen yield on photoexcitation of the homoleptic dinuclear Ru^{II}(dppz) complex was very low (~4%), the comparable estimate for $\mathbf{12}^{4+}$ was almost 70%. Interestingly, for $\mathbf{13}^{4+}$, an intermediate figure of ~16% was obtained even though this complex still displayed a DNA light-switch effect. These latter observations are consistent with occupation and equilibration between a dppn-based ^{3}ππ* state and a shorter lived Ru^{II}dppz-based ^{3}MLCT state.

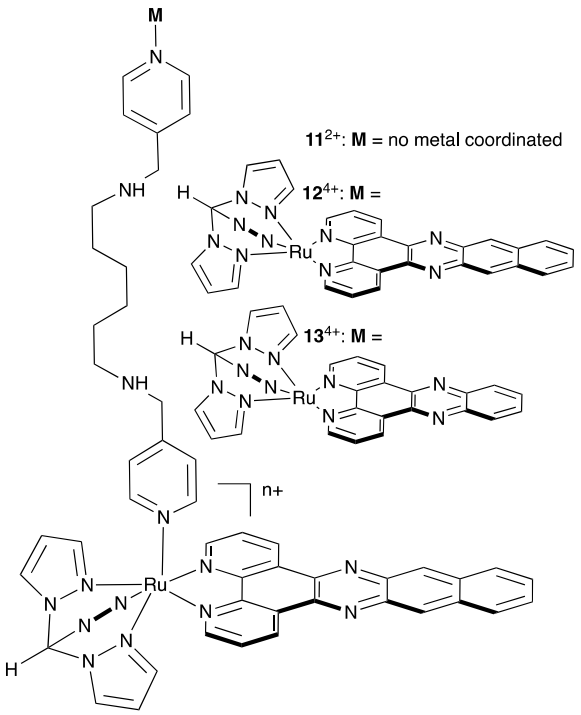

Fig 7 Structure of mono and dinuclear complexes containing the Ru^{II}(dppn) fragment used in PDT studies.

The live cell uptake properties of these complexes were also surprisingly different. In cell ruthenium concentrations after exposure to each complex were directly measured using inductively coupled plasma mass spectrometry (ICP-MS). This analysis revealed that although all three complexes are internalized by cells, the intracellular accumulation of both dinuclear ruthenium complexes are notably higher than that of the mononuclear complexes. Interestingly, while the uptake of heteroleptic complex $\mathbf{21}^{4+}$ is around x7 that of $\mathbf{19}^{2+}$ the comparable figure for homoleptic complex $\mathbf{20}^{4+}$ is x65. This indicates that the lower charge density and higher lipophilicity of the oligonuclear systems relative to the mononuclear complex are determinants of uptake. The luminescent properties of $\mathbf{20}^{4+}$ were exploited to investigate its intracellular localisation through confocal laser scanning microscopy, CLSM, which revealed that the complex localizes within mitochondria and particularly lysosomes – Fig 8.

As expected from their live cell uptake and high singlet oxygen sensitization properties the complexes are promising leads for photodynamic therapy, PDT. Studies involving the A2780 human ovarian cancer line showed that all three complexes are phototoxic, but - perhaps due to its better uptake properties - complex $\mathbf{20}^{4+}$ has the most potent activity; even using low light fluences (14 J cm^{-2}) the complex displays a phototoxic index (PI) of >200. Interestingly, these effects are potentiated in the related cisplatin-resistant A2780cis cell-line, in which PIs of up to 1000 were observed. These promising studies suggest that derivatives of $\mathbf{20}^{4+}$ and $\mathbf{21}^{4+}$ could be exploited as PDT sensitizers, particularly if they can be adapted to be photo-excited with lower energy light sources that provide high tissue penetration.

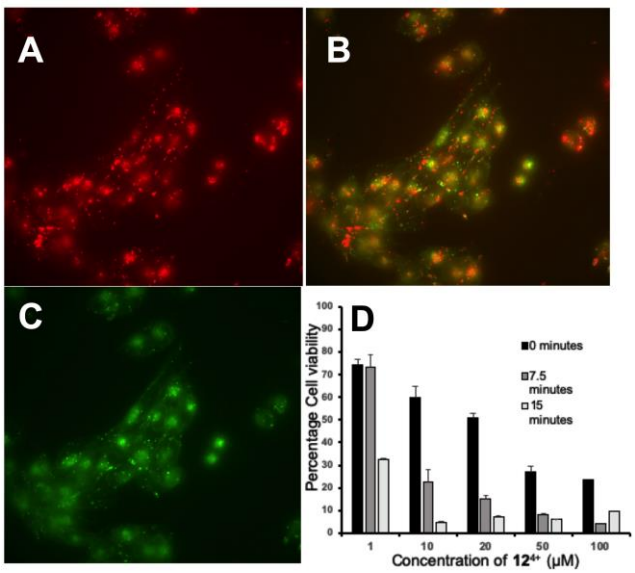

Fig 8. A: A2780 cells showing emission from [**13**]Cl_4, B: Emission from lysotracker deep red C: Merged co-localization image. E: A2780 cell viability data for complexes [[**12**]Cl_4, upon irradiation. Adapted with permission from reference 57.

Dinuclear tpphz complexes as imaging probes

Apart from using a modular approach in the construction of linked M(dppz) systems, we have also developed complexes incorporating the ditopic briding ligand tetrapyridyl[3,2-a:2′,3′-c:3″,2″-h:2‴,3‴-j]-phenazine (tpphz). In these studies the photophysical and biological properties of rigid MtpphzM units are modulated by the choice of metal ion and nature of the ancillary ligands coordinated to the two metals. This work first began through the aim of developing a light-switch complex for a specific non-canonical DNA structure.

The first quadruplex DNA light-switch.

It has been known for many years that in the right conditions G-rich DNA can form four-stranded structures[58] but over the last two decades the structure and possible functions of such quadruplexes within living cells have attracted more and more attention. [59-62] Current studies indicate that quadruplex structures are ubiquitous within cells and they have been associated with an almost bewildering range of functions including; determination of Hayflick limits, replication initiation, transcription switching, epigenetics, and genetic disease. However, there are still many unanswered questions on the in-cell occurrence, dynamics, and function of these fascinating structures.

When we first began our work in this area the presence of quadruplexes within a cell environment was still a moot point. So, the idea of a probe that produced a distinctive signal only when bound to a quadruplex structure was an attractive goal and it seemed possible that an adapted DNA light-switch complex might just meet these requirements.

A consideration of the distinctive structure of the G-tetrad that forms the basis of all quadruplexes, led to the conclusions that a more extended version of the dppz ligand would provide an appropriate aromatic stacking surface, whilst a dinuclear Ru^{II} complex would provide cationic centres to coulombically interact with the anionic phosphate residues of the quadruplex backbone. Using these simple selection criteria, a small group of previously reported complexes - in particular $\mathbf{14}^{4+}$ and $\mathbf{15}^{4+}$, Fig. 9,[63] which incorporated the tpphz - were identified as potential leads.

Studies on this small library revealed that when $\mathbf{14}^{4+}$ and $\mathbf{15}^{4+}$ bind to duplex DNA they display a light-switch effect in which a broad emission band at ~670 nm increases by ×60.[64] Their emission properties on exposure to quadruplex structures are more complex.

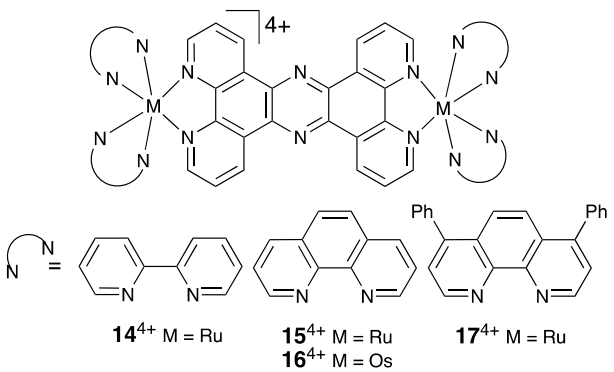

Fig 9 Dinuclear complexes investigated as DNA Probes

Although the complexes display virtually no increase in emission on binding to structures with lateral loops, binding to quadruplex structures containing external lateral loops is accompanied by a ×150 increase in emission intensity which is also blue shifted to ~635 nm. Analysis of these luminescence changes also reveals a range of binding properties. Whilst the complexes bind to duplex DNA with affinities of ~10^6 M^{-1}, equivalent figures for their interactions with quadruplexes vary over three orders of magnitudes. For example, binding of $\mathbf{14}^{4+}$ to the thrombin binding aptamer – an unimolecular structure with a single lateral loop - results in a estimated K_b of ~10^4 M^{-1} but its affinity for the antiparallel-folded human telomere structure, HTS, is >10^7 M^{-1}.[65] Consequently, the molecular basis for these distinctive selectivities was investigated

We initially suggested that the complexes may intercalate into duplex DNA,[64] perhaps through the threading interaction first reported by Lincoln and Nordén in their investigations on their similar, more extended, analogues. However, later studies by Dunbar and Turro demonstrated that $\mathbf{14}^{4+}$ does not spontaneously intercalate into genomic duplex DNA, even when added to single stranded DNA as it anneals into a duplex, indicating that the complexes groove-bind to extended double-stranded sequences.[66]

Very recently, we carried out detailed NMR experiments on the interaction of the three individual stereoisomers of $\mathbf{14}^{4+}$ with the octanucleotide duplex sequence; d(GCATATCG).d(CGATATGC). Surprisingly, we found that the Λ,Λ and Δ,Λ isomers bound to the centre of the octanucleotide by threaded intercalation– Fig 10A; yet, the Δ,Δ form displayed two bound states in intermediate exchange on the NMR timescale, suggesting a dynamic exchange between minor groove binding and intercalation. We concluded that although the complex does groove bind to stable duplexes, it is capable of threading into less stable, or more flexible, sequences.[67]

Similar experiments revealed that chirality is also an important factor in the interaction of these complexes with the antiparallel HTS sequence d[$AG_3(TTAG_3)_3$]. Prompted by the observation that Δ,Δ-$\mathbf{15}^{4+}$ binds to HTS with a relatively low affinity ($K_b = 3 \times 10^5$ M^{-1}), but K_b for Λ,Λ-$\mathbf{15}^{4+}$ is >10^7 M^{-1}, a combined NMR and computational analysis using $\mathbf{14}^{4+}$ showed that while both Δ,Δ-$\mathbf{14}^{4+}$ and Λ,Λ-$\mathbf{15}^{4+}$ bind to HTS by stacking onto the G-tetrad at the lateral loop end of the structure, only the Λ,Λ stereoisomer can thread through the diagonal loop over the tetrad at the other end of the quadruplex - Fig 10B. Hence, it was concluded that this threading interaction is responsible for the higher HTS-binding affinity of the Λ,Λ stereoisomer.[68] CLSM studies on the cell uptake of $\mathbf{14}^{4+}$ and $\mathbf{15}^{4+}$ also produced striking results.

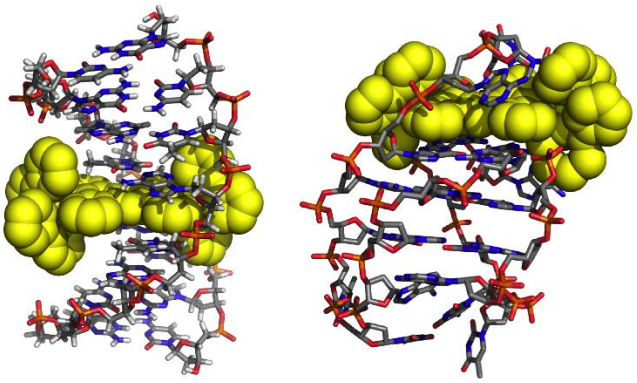

Fig. 10 Left: NMR-based structure for the major conformation of $\mathbf{14}^{4+}$ threaded into the duplex sequence d(GCATATCG)$_2$. Right: NMR-based structure of $\mathbf{14}^{4+}$ threaded into the HTS d[$AG_3(TTAG_3)_3$] sequence folded into an antiparallel quadruplex . Adapted with permission from references 67 and 68, respectively.

Initial experiments, with complex $\mathbf{14}^{4+}$, produced disappointing results as this complex is only internalized by fixed or dead cells. Remarkably, however, in the same conditions $\mathbf{15}^{4+}$ is rapidly taken up by commonly used cultures such as MCF-7, CHO, and A2780 cell-lines, but displays very low cytotoxicity (IC_{50} after 24 hours = 138 μM). Furthermore, binding to nuclear DNA was revealed in

CLSM images demonstrating that, thanks to its DNA light-switch response, **15**$^{4+}$ is an excellent luminescent probe for chromatin - Fig 11.

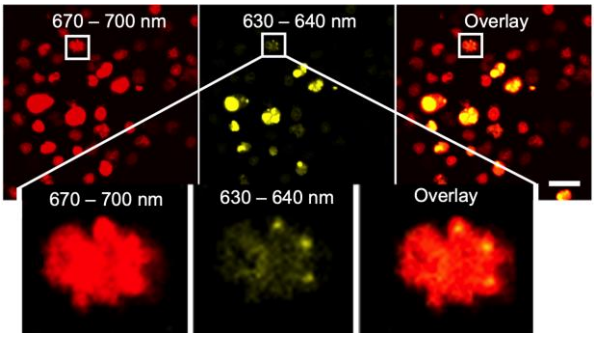

Fig. 11 Confocal microscopy images using two separate detection channels 670-700 nm (red) and 630-640 nm (yellow) show the multiple emission profile of nuclear luminescence from L5178Y-R cells (which have extended G-rich telomeric DNA) stained with **15**$^{4+}$ Top Left: 670-700 nm channel Top middle: 630-640 nm channel. Top Right Overlayed image. Bottom: L5178-R metaphase cells with chromosomes showing specific localisation of the 630-640 nm emission peaks. Adapted with permission from reference 69.

Indeed, the complex is well suited to this application: as it is chemically and photochemically stable it does not photo-bleach and its large Stokes shift - with an emission in the red/NIR - reduces "crosstalk" from the excitation source and endogenous luminophores. Co-localization studies with the general nucleic acid probe, SYTO 9, confirmed that the complex images DNA but not RNA and it was also found that the complex is internalized by an energy-dependent mechanism that does not involve endocytosis or pinocytosis. [69]

More interestingly still, lambda-stacking experiments showed that the internalized complex displayed two emission maxima - centred at ~680 nm and ~630 nm respectively - which correlated with the duplex and quadruplex light-switch effects in cell-free studies. By defining separate 670–700 nm and 630–640 nm channels it became clear that the red-shifted emission was consistent with general chromatin staining, but the blue-shifted emission was from specific areas within nuclei and did not co-localize with the other channel. Several experimental lines, including imaging cells lines with differing telomere lengths, provided evidence that this distinctive higher-energy emission is a marker for quadruplex DNA within live cells – Fig 11.

TEM Probes.

The most commonly employed contrast stain for TEM is a far-from-ideal reagent. Osmium tetroxide is used to visualise intracellular structure as it densely stains membranes. However, it is extremely toxic and highly volatile; even at very low exposures (0.1 mg/m^3) it can cause visual disturbances, headaches, and even conjunctivitis, yet alternative TEM stains are virtually unreported.

As complex **15**$^{4+}$ contains two electron-dense Ru^{II} ions, it seemed likely that the complex or derivatives could have considerable potential as a contrast stain for this technique. An added attraction of such complexes is their handling convenience. In contrast to OsO_4., **15**$^{4+}$ and its derivatives have very low toxicities, possess low reactivity and volatility, and display excellent water solubility Studies on cells treated with **15**$^{4+}$ confirmed that the intracellular localisation of the complex at high spatial resolution can be determined through TEM;[69] however, to obtain enhanced TEM imaging capabilities, its Os^{II} derivatives, **16**$^{4+}$ (Fig 9) was investigated. Consistent with the energy gap law, due to its lowered excited state energy, this complex$^+$ is non-emissive; however, the inclusion of two third row transition metal ions means that it is an even more effective contrast stain than its Ru^{II} analogue.

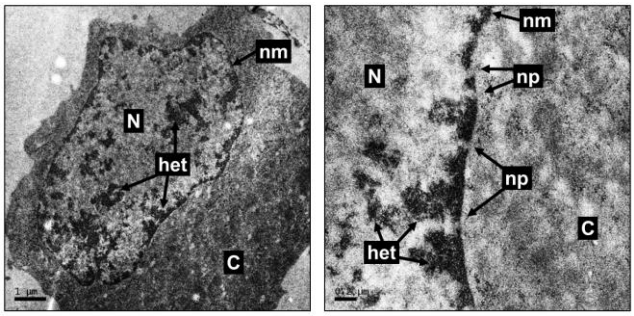

Fig. 12 Left: TEM image of a MCF7 cell nucleus stained with **16**$^{4+}$. Right: Detailed image of nuclear membrane structure, showing nuclear pore complex. Key: pm = plasma membrane, nm = nuclear membrane, N = nucleus, C = cytosol, n = nucleolus, m = mitochondria, het = hetrochromatin, np = nuclear pore complex. Adapted with permission from reference 70.

It was found that staining was achieved in previously fixed cells but also in live cells that were fixed after treatment with the complex. In either case, cells stained with **16**$^{4+}$ display excellent levels of intracellular contrast, which facilities the visualisation of cellular detail at resolutions entirely comparable to those obtained by OsO_4. For example, visualisation of nuclear pore complexes (~120 nm) which are responsible for transport of molecules across the nuclear membrane are clearly visualized – Fig 12. [70]

It was also found that the subcellular localisation of **14**$^{4+}$ - **16**$^{4+}$ can be selected for by judicious selection of ancillary ligands. A derivative of the parent complexes, **17**$^{4+}$ (Fig 9), containing the 4,7-diphenyl-1,10-phenanthroline, DIP, was designed to localize within lipid rich, membrane structures. The inclusion of this ligand has two effects. First, the greater steric bulk of DIP inhibits the ability of the complex to groove-bind with duplex DNA resulting in a lower binding affinity compared to **14**$^{4+}$ and **15**$^{4+}$. Second, the ligand increased the lipophilicity of **17**$^{4+}$, which was demonstrated in cell-free experiments using liposomes. The complex demonstrated a clear increase in luminescence when interacting with liposomes, whereas **15**$^{4+}$ displayed no equivalent change in luminescence. Consequent CLSM studies with fixed cells revealed that MCF7 cells exposed to **17**$^{4+}$ displayed pronounced staining of the nuclear membrane and perinuclear space, whilst detailed immunofluorescent co-staining techniques confirmed the complex preferentially stained the lipid-rich endoplasmic reticulum over the Golgi apparatus – Fig 13.[71]

Of course, an additional advantage of **17**$^{4+}$ over conventional ER probes is its additional function as a TEM contrast stain and experiments using this technique showed that it could also be used to image mitochondrial inner membrane structure. However, this change in subcellular localization was accompanied by a concomitant increase in live-cell cytotoxicity.

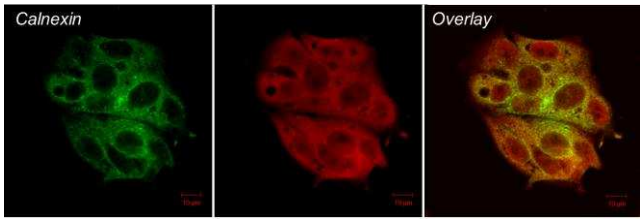

Fig. 13 Co-staining of MCF7 cells Left: ER-localized Calnexin protein visualized by immunofluorescence (FITC-conjugated secondary antibody) Centre: emission from **17**$^{4+}$ Right: merged images. Adapted with permission from reference 71.

Exploring charge effects in localisation

In the last two decades, research into polypyridyl Ir^{III}-based complexes for a variety of light-driven applications has rapidly grown. Thanks to large spin-orbit coupling effects these luminophores possess high triplet state conversion efficiencies. Moreover, by coordinating conventional and cyclometalating ligands to the Ir^{III} centre, mixing of MLCT and LLCT (ligand-to-ligand charge-transfer) states can occur, thereby providing a method to tune the excited state properties of these systems.[72] Yet, when we began our work, there were surprisingly few examples of DNA targeting Ir^{III} cell probes, probably due to the poor aqueous solubility of cyclometalated systems, which commonly possess low cationic charge. To address this issue, we synthesized heteronuclear $Ir^{III}Ru^{II}$ complexes. By incorporating cyclometalated ligands complexes that are isostructural with **14**$^{4+}$ and **15**$^{4+}$ but with lower overall charges could be obtained. Using this approach, **18**$^{3+}$, **19**$^{3+}$, and **20**$^{3+}$ were obtained - Fig 14.[73,74]

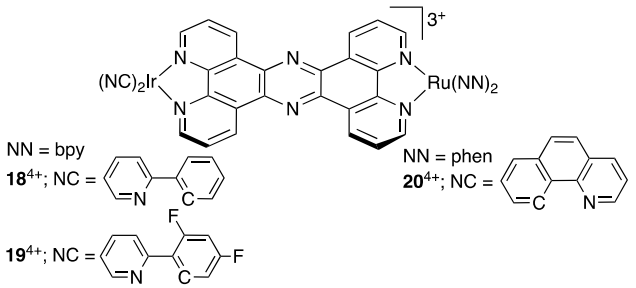

Fig 14 Structures of $Ir^{II}Ru^{II}$ complexes **18**$^{3+}$ - **20**$^{3+}$ with modified uptake properties compared to **15**$^{4+}$.

Although their emission properties are similar to their $Ru^{II}Ru^{II}$ analogues - indicating that the lowest excited state of these complexes is centred on their $Ru(bipy)_2(tpphz)$ moiety - they have very different biophysical and cell uptake properties. Two of the complexes (**18**$^{3+}$ and **19**$^{3+}$) bind to duplex DNA with affinities that are an order of magnitude lower than **14**$^{4+}$ and **15**$^{4+}$, suggesting that Coulombic effects play a significant role in these interactions.[73] Yet, the estimated binding parameters for complex **20**$^{3+}$ are very similar to those of **15**$^{4+}$. This suggests that the additional hydrophobic and/or stacking interactions provided by the more extended and rigid ancillary ligands of **20**$^{3+}$ delivers key additional contributions to the binding thermodynamics of this complex.[74]

A CLSM comparison of the cell uptake properties of **14**$^{4+}$, **18**$^{3+}$ and **19**$^{3+}$, which are close structural analogues, is particularly interesting. Unlike **14**$^{4+}$ both **18**$^{3+}$ and **19**$^{3+}$ *are* internalized by live HeLa cells and function as luminescent stains for chromatin. These facts suggest that the lower charge of the heterometallic species facilitate cellular uptake, particularly as cells are brightly stained at concentrations that are lower than those required for imaging by **15**$^{4+}$. Importantly, in contrast to many examples where increased lipophilicity is accompanied by a change in sub-cellular targeting, *vide infra*, this improved cellular uptake occurs without loss of nuclear localisation Moreover, analysis of luminescent intensities indicates that complex **19**$^{3+}$, which contains fluorinated ancillary ligands, shows improved uptake and nuclear localisation compared to its non-fluorinated analogue.[73] This observation is an example of a well-known effect exploited in classical medicinal chemistry, in which fluorination is used to increase the cell permeability of a pharmaceutical.

However, the combination of lowered charge and the more rigid, extended ancillary ligands of **20**$^{3+}$ do begin to affect its biomolecular targeting properties. Whilst the complex does very effectively stain nuclear DNA in fixed cells, initial attempts at live cell staining produced very disappointing results as incubation of MCF7 cells with the complex for periods as long as 24 hours resulted in poor, non-specific intracellular emission and no nuclear staining. This effect was found to be caused to one of the components of the culture the cells were grown in.

A number of metal complexes have been shown to interact with serum proteins, and some have even been developed as optical probes for serum albumins. As bovine serum albumin, BSA, is a ubiquitous constituent of cell cultures its interaction with **20**$^{3+}$ in cell-free conditions was investigated. It was found that this complex bound to Sudlow site I of BSA, a hydrophobic cavity which is known to bind hydrophobic drugs. Subsequent exposure of cells to low concentrations of **20**$^{3+}$ in serum-free conditions resulted in rapid uptake of the complex and CLSM revealed well-defined nuclear localisation, but there was also a concomitant increase in the apparent cytotoxicity of the complex.[74]

As pointed out in the original report, these observations have implications for the design of potential therapeutics and imaging probes; structural changes aimed at increasing permeability through enhanced lipophilicity may actually adversely affect the ability of such agents to reach their therapeutic targets when they are surrounded by blood serum proteins.

Exploiting advanced imaging techniques

Thanks to diffraction effects first described by Abbé, all optical microscopy techniques, including CLSM - which offers considerable improvements signal-to-noise and resolutions compared to conventional epifluorescence microscopy - have spatial resolutions restricted to half the wavelength of their imaging light. In recent years, several novel techniques have been developed to address these drawbacks and recent reports from our lab has shown how **15**$^{4+}$ can be used as a probe for several of these emerging techniques.

Lifetime based, time-resolved emission imaging microscopy, TREM, offer several advantages over conventional intensity-based technologies as it provides information on the probe environment independent of its concentration. Furthermore, if TREM employs phosphorescence probes that emit on the hundreds of nanoseconds to microsecond timescale, this technique completely removes interference from biomolecular autofluorescence which typically has lifetimes from picosecond to <10 nanoseconds. Two-photon absorption, 2PA, microscopy is another technique that offers several advantages over conventional optical methods. As 2PA is

dependent on the square of light intensity, excitation of probes is highly focused, resulting in excellent spatial resolution. Furthermore, 2PA microscopy is particularly attractive for live cell-based samples as low-energy excitation wavelengths within the biological optical window can be used. Through the identification of probes with suitable properties, the advantages of these two modalities can be combined in TPA-TREM. As the ^{3}MLCT-based light-switch effect demonstrated by **14**$^{4+}$ and **15**$^{4+}$ leads to increases in emission lifetime as well as intensity, it seemed likely that they could function as lifetime probes for intracellular DNA.

The 2PA cross-sections, σ, for both complexes was found to be appreciable, with estimated values of σ =108 GM for **14**$^{4+}$ and σ =142 GM for **15**$^{4+}$ being obtained; values that comparable with other Ru^{II}-based complexes specifically synthesized to display high 2PA cross sections. These encouraging results prompted us to undertake lifetime microscopy studies under 2PA conditions. [75]

In live MCF-7 or HaCat cells treated with **15**$^{4+}$ and excited with 800 nm light in a 2PA regime, emission from nuclei displayed a characteristic lifetime of 175 ns – Fig. 15A. Metaphase spreads of chromosomes derived from HeLa stained with either **22**$^{4+}$ and **23**$^{4+}$ allowed visualization of condensed chromosomal DNA with recorded lifetimes being in excellent agreement with those from live cells, indicating that in both environments the complexes are bound to DNA in the same way. Intriguingly, detailed analysis of the intracellular data from the complexes in fixed and live cells revealed a second shorter emission life-time (110 nm for **15**$^{4+}$) localised within the cytoplasm, implying a specific binding site within this region – Fig. 15B. The longer lifetime from the nucleus implies that protection from surrounding water molecules in DNA-bound sites is more effective than in the cytoplasm and explains why cytosolic emission was not observed through confocal microscopy; exposure to bulk water will increase excited-state quenching of the complexes producing greatly reduced emission quantum yields and intensities. These experiments illustrate how new information can be derived from lifetime imaging techniques. The identity of the cytoplasmic signal was subsequently determined using super-resolution microscopy, SRM.

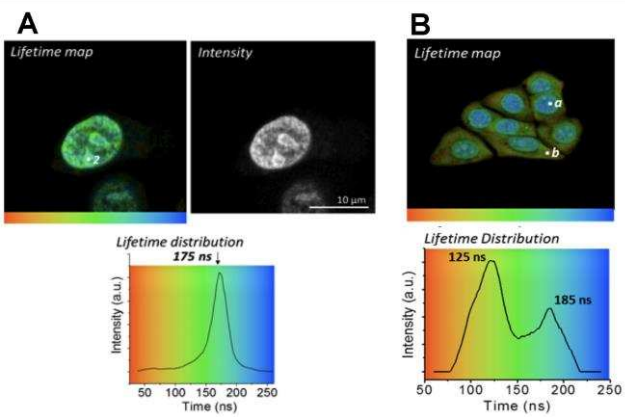

Fig 15 A. A comparison of lifetime and intensity imaging of live MCF-7 cells pretreated with complex **15**$^{4+}$ showing single nuclear lifetime B. Lifetime imaging of fixed, permeabilized MCF7 cells treated with complex **15**$^{4+}$ showing different lifetimes in the nucleus(a) and cytoplasm(b). Adapted with permission from reference 75.

One approach to SRM is stimulated emission depletion (STED) microscopy. In STED, selective deactivation of a photo-excited dye molecule using a depletion beam can provide excellent spatial resolution (below 30 nm), but does require a luminophore with high photostability.[76] Given the known photo-stability of luminescent Ru^{II} complexes, we investigated the application of **15**$^{4+}$ for SRM.

A series of TEM and optical imaging experiments revealed, that apart from nuclear staining, the complex is also internalized within the inter-membrane space of mitochondria. In fact, at lower treatment concentrations (<10 µM) **15**$^{4+}$ exclusively localizes within mitochondria. As **15**$^{4+}$ displays a low phototoxicity even under continuous irradiation, has a long-lived emission (which increases the probability of stimulated emission), and a large Stoke Shift (which minimizes self-quenching even at high dye loading), its use as a STED probe was also investigated. [77]

Through a collaboration with Jorge Bernardino de la Serna at RAL (now at Imperial College, London), we found that by using a 775 nm depletion beam excellent STED images of suitably treated live cells could be produced. At low concentrations (~6 µM) specific imaging of mitochondria were successfully accomplished at resolutions <50 nm and at higher concentrations striking images of chromatin were obtained, and resolutions below 50 nm were still maintained – Fig 16 A - C.

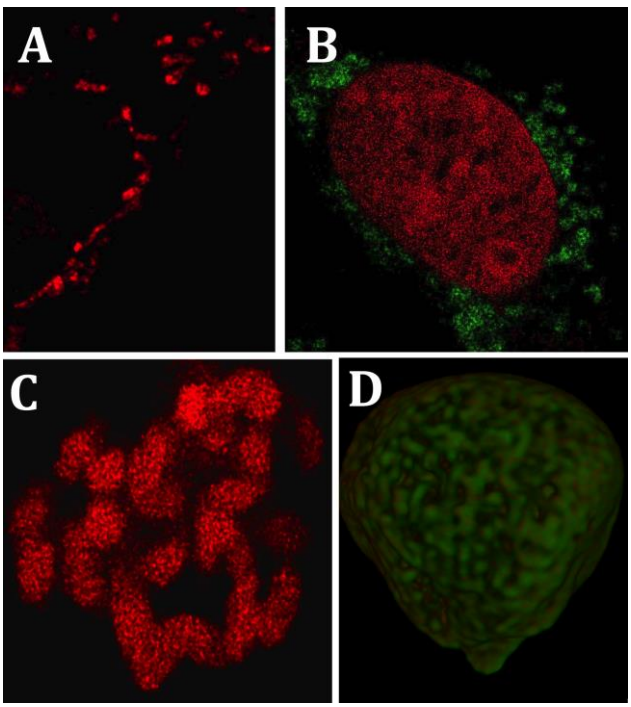

Fig 16 A. STED image showing staining of mitochondria in a MCF7 cell at low **15**$^{4+}$ concentration B. STED image of a single cell showing chromatin staining by **15**$^{4+}$ at higher concentration (red), with mitochondria co-stained by a mitotracker dye (green). C. Magnified STED image showing chromosomal details D. 3D-STED super-resolved reconstruction of a single whole A2780 cell nucleus. Adapted with permission from reference 77.

With these successes in hand, the use of **15**$^{4+}$ in 3D-STED was investigated. This method requires highly photo-stable probe as the optical sectioning used to generate 3D images means that it must be photostable under prolonged irradiation – conditions that often lead to photobleaching of most conventional probes. The high photostability of **15**$^{4+}$ under high photon fluxes proved to be a key

feature in obtaining 3-D images of entire organelles at STED resolutions. This was illustrated by a full reconstruction of a *single* nucleus that required 165 individual section planes, producing excellent resolution in all three axes (XY resolutions ≈ 35 nm and 120-150nm in the Z-axis) – Fig. 16D.

Having established the versatile in-cell imaging capabilities of $\mathbf{14}^{4+}$ and $\mathbf{15}^{4+}$ and their derivatives, the possibility of developing related complexes that also displayed therapeutic action was also investigated. These studies were inspired by the hope of identifying and developing genuine theranostics.

Therapeutic leads from tpphz complexes

Anticancer therapeutic leads.

Because complexes like $\mathbf{14}^{4+}$ and $\mathbf{15}^{4+}$ possessed such interesting cell uptake properties, their mononuclear analogues were also investigated. Although the DNA light-switch properties of $\mathbf{21}^{2+}$, Fig. 17, was first reported by Tysoe, *et al* in 1999,[78] no consequent cell studies had been reported. Our initial studies on this complex and its phen analogue, $\mathbf{22}^{2+}$, yielded some surprising results.

Unlike the dppz-based parent complexes, both $\mathbf{21}^{2+}$ and $\mathbf{22}^{2+}$ are live-cell permeant, although $\mathbf{22}^{2+}$ displays much more efficient nuclear staining, even at low concentrations.

As both complexes brightly stain chromatin in fixed cells, it seems that the reduced luminescence of $\mathbf{21}^{2+}$ observed in live cells is due to its poorer cellular uptake compared to $\mathbf{22}^{2+}$. More importantly, we found that the complexes are cytotoxic toward the A2780 human ovarian cancer cell-line and, crucially, not only is the potency of $\mathbf{22}^{2+}$ comparable to cisplatin, but its potency is retained in the cisplatin-resistant A2780cis daughter cell-line. [79] Recently, more detailed studies involving $\mathbf{22}^{2+}$ cast light on its mechanism of action.

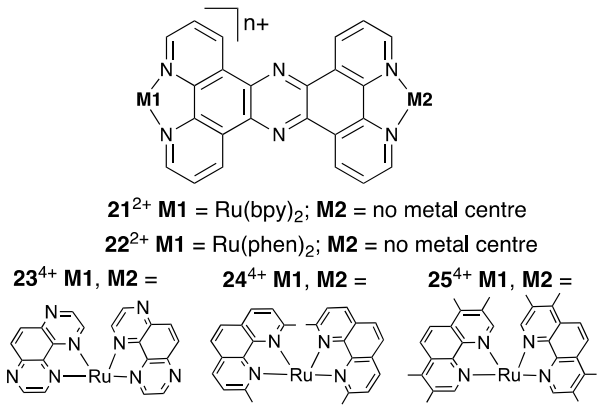

Fig. 17 Structures of mono- and dinuclear complexes containing the tpphz ligand that have been developed as therapeutics.

Proteomic analysis of cytotoxicity

A comparison of $\mathbf{22}^{2+}$ with non-intercalating mono- and dinuclear derivatives incorporating tpphz and a related ligand, showed that only $\mathbf{22}^{2+}$ displayed high therapeutic potency against both A2780 and A2780cis cells and, encouragingly, equivalent IC50 figures in the non-tumour HEK293 cell-line were found to be over two orders of magnitude higher than the values found for A2780cis cells. Inductively coupled plasma mass spectrometry (ICP-MS) experiments on $\mathbf{22}^{2+}$ and its derivatives showed that therapeutic activity was not simply a function of cell uptake concentration.as some of the less potent complexes were internalized at higher concentrations than $\mathbf{22}^{2+}$. Furthermore, despite all the complexes displaying considerably lowered cellular accumulation in A2780CIS cells compared to the parent line - consistent with previous studies indicating that A2780CIS cells possess enhanced efflux capabilities – complex $\mathbf{22}^{2+}$ still retains its potency.

Studies into the mechanism of cell death on exposure to $\mathbf{22}^{2+}$ revealed a non-apoptotic mechanism, probably involving oncosis. This is significant as intrinsic or acquired chemotherapy resistance often involves abrogation of apoptotic pathways; indeed, as a result of this phenomenon one-third of all solid cancers respond poorly to current treatments. To further explore the effects of exposure to $\mathbf{22}^{2+}$ a proteomic analysis on A2780CIS cells treated with the complex was carried out using Stable Isotope Labelling by Amino Acids in Cell Culture (SILAC), By accurately quantifying changes in protein expression through a ratiometric method based on mass spectrometry SILAC provided a detailed picture of the cellular response to $\mathbf{22}^{2+}$.

Of the 3400 distinct proteins identified by SILAC, the abundance of 42 proteins was significantly altered on exposure to the complex, with 32 up-regulated, and 10 proteins down-regulated. A significant fraction of these proteins are associated with processes involved in DNA replication, DNA repair, or checkpoint signalling associated with replication stress, but the largest group of proteins with altered expression levels are involved in cellular or mitochondrial responses to reactive oxygen species and general oxidative stress. These data indicate the complex provokes both DNA damage *and* oxidative stress responses in treated cells. This is significant because it is established that therapeutic regimes displaying more than one mechanism of action are less susceptible to conventional resistance mechanisms. Given this, and the fact that $\mathbf{22}^{2+}$ induces a non-apoptotic death pathway, it was concluded that this complex and its analogues offer great potential as novel anticancer therapeutics.[80]

Radio-sensitising action.

One therapeutic target for this class of complexes was identified to be oesophageal cancer. Treatment of this condition is challenging as 77% of oesophageal cancers lack p53 function, reducing or abrogating apoptosis as a response to DNA damage. Accordingly, therapeutics that induce non-apoptotic death mechanisms may be more effective treatments for oesophageal cancers.

Through a collaboration with Katherine Vallis's group involving Martin Gill - an ex-member of the Thomas group - these facts led to an exploration of the effects of $\mathbf{22}^{2+}$ on p53-deficient oesophageal cancer cells. These studies revealed that exposure to $\mathbf{22}^{2+}$ at its IC_{50} concentration led to pronounced and rapid DNA replication inhibition and - as observed in A2780 and A2780CIS cells – the complex only provoked low levels of apoptosis in OE21 cells. Fascinating morphological changes in treated cells going through cell division were also observed. The complex induced chromosome misalignment and the formation of multiple micronuclei, indicating that the DNA damage accumulated during mitosis causes errors in chromosome segregation and attachment. Another promising observation was the complex displayed

significantly reduced activity against non-proliferative immortalised human small airway epithelial cells.

The application of $\mathbf{22}^{2+}$ as a radiosensitizer was then explored. It was found that, at a concentration of only 2 μM, significant decreases in surviving cell fractions compared to radiation alone occurred, accompanied by a substantial increase in double strand break formation compared to single treatment regimes.[81]

Consequently, this work was extended through the use of nanoparticles containing Auger electron emitting ^{111}In centres designed to bind to epidermal growth factor receptor, EGRF, a membrane-bound receptor over- expressed in almost 70% of oesophageal tumours. Studies on such systems confirmed that they are preferentially taken up by EGRF-overexpressing oesophageal cancer cells compared to normal human fibroblasts, displaying the expected radio-toxicity. When these nanoparticles were also loaded with $\mathbf{22}^{2+}$supplied by our lab these effects were more pronounced as the contributions of the ^{111}In Auger electron emitter and radiosensitizer were additive.[82]

Toward novel phototherapeutics

Pioneering work by the Kirsch-De Mesmaeker and Kelly groups demonstrated that coordination of electron-deficient ligands, such as 1,4,5,8-tetraazaphenanthrene (TAP), on to Ru^{II} centres results in complexes that possess highly photo-oxidizing $Ru^{II}\rightarrow$TAP ^{3}MLCT excited states.[83] The biophysical and photophysical properties of $[Ru(TAP)_2dppz]^{2+}$ have proven to be of particular interest. As might be expected this complex binds to DNA through minor groove intercalation in a manner that that closely related to $[Ru(phen)_2dppz]^{2+}$. However, instead of displaying a light-switch effect, $Ru(TAP)_2dppz]^{2+}$ is luminescent in water and - due to photo-redox reactions involving the oxidation of guanine sites - its emission is quenched in the presence of DNA.[84] This phenomenon has been used to probe DNA photodamage processes in exquisite detail[85] and it could, potentially, form the basis of novel sensitizers for PDT. Unfortunately, $Ru(TAP)_2dppz]^{2+}$ displays poor cell penetration; for example, even after HeLa cells are exposed to the complex for 24 hours it is only found in their cytoplasm.[86]

To address this problem, we synthesized an iso-structural derivative of $\mathbf{15}^{4+}$ containing $Ru^{II}(TAP)_2$ fragments, $\mathbf{23}^{4+}$, Fig. 17, in the hope that it would display the same cell uptake/localisation properties as the parent complex, but display photophysical properties that were more related to $Ru(TAP)_2dppz]^{2+}$.[87]

A combination of electrochemical and photophysical experiments along with DFT calculations, Fig 18A, revealed that photo-excitation of $\mathbf{23}^{4+}$ yields a $Ru^{II}\rightarrow$TAP ^{3}MLCT state, which is emissive in organic and aqueous solutions, but is quenched by the addition of any nucleotides containing guanine sites such as GMP, as well as duplex and quadruplex DNA. Further optical studies revealed that the complex binds duplex DNA with an affinity that is similar to its parent compound. Although its binding to quadruplex was reduced compared to $\mathbf{15}^{4+}$ – presumably due to unfavourable interactions between the TAP ancillary ligands and external loop of this structure – a K_b of >5 x10^5 M^{-1} was still observed in the high salt concentrations required for quadruplex folding. Significantly, transient absorption spectroscopy revealed that photoexcitation of $\mathbf{23}^{4+}$ in the presence of quadruplex DNA and G-site-containing duplexes resulted in the emergence of a signal at 515 nm characteristic of the guanine radical cation generated through photo-oxidation by the $Ru^{II}\rightarrow$TAP ^{3}MLCT excited state - Fig 18B. Given these exciting results, the cell uptake properties of the complex were investigated.

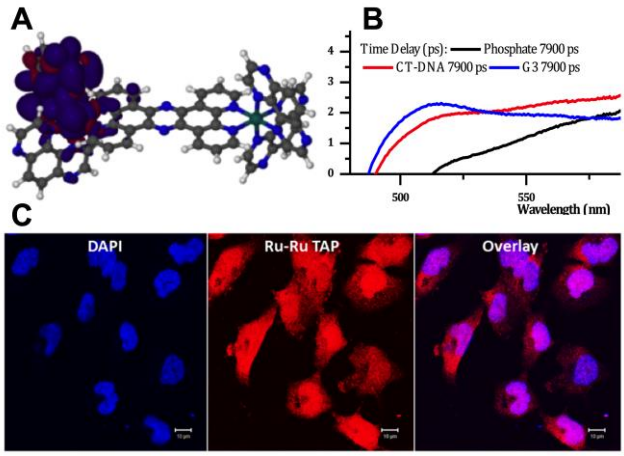

Fig. 18 A: Lowest triplet structures for $\mathbf{23}^{4+}$ in MeCN. B: Selected transient absorption spectra for $\mathbf{23}^{4+}$ in phosphate buffer with and without CT-DNA and quadruplex folded HTS, showing the growth of the transient band at ~515 nm after 7900 ps in the presence of DNA. C:Co-staining with DAPI reveals that $\mathbf{23}^{4+}$ penetrates into the nucleus of malignant melanoma cells. Adapted with permission from reference 87.

These studies focussed on melanoma - an aggressive cancer that can produce fatality rates high as >90%. As it displays a range of therapeutic resistance mechanisms, new treatments for melanoma are urgently needed and it has been suggested that PDT could be efficacious in this role. Therefore, in collaboration with Sheila MacNeil and John Haycock, the phototoxicity of $\mathbf{23}^{4+}$ toward human melanoma C8161 cells were investigated. As this line is highly invasive and spontaneously metastatic it represented a therapeutically relevant and challenging treatment target. [87]

The complex was found to be cell permeant and co-staining with standard cell probes revealed that it largely localizes within the nuclei of live C8161 cells (Fig 18C), though some staining of mitochondria and lysosomes – organelles which are also targets for PDT - was also observed. In the dark, at a range of concentrations up to 200 μM, $\mathbf{23}^{4+}$ had no detectable effect on cell viability; yet, irradiation at low fluences (up to a maximum of only 18 J cm^{-2}) resulted in a huge drop in viability, reaching zero in optimal conditions. These observations confirm that $\mathbf{23}^{4+}$ could be successfully "re-engineered" to produce a novel phototherapeutic. By using a similar approach, antimicrobial theranostics were also identified.

Antimicrobial theranostics

The rapid emergence of antimicrobial resistance, AMR, is currently one of the greatest challenges facing healthcare globally. In a post-antibiotic age, a third of deaths could once again be attributed to untreatable infections and it has been projected that by 2050 AMR could be responsible for an additional 10 M fatalities *per annum*.[88] Pathogenic Gram-negative bacteria present a particular challenge; no new class of antibiotics for these pathogens has been approved for over 50 years and only one new compound has entered Phase 1 trials in the last 20 years.[89]

Perhaps surprisingly, the antimicrobial activity of certain polypyridyl Ru^{II} complexes was established almost 70 years ago. In work before its time, the Dwyer group first showed that Ru^{II}

complexes containing methylated phen ligands are active against a range of bacteria, particularly Gram-positive species.[90] With the emergence of AMR, such structures are being reinvestigated as therapeutic leads.[91] The fact that oligonuclear analogues of the Dwyer's original lead were found to display higher activity and appear to target bacterial cell membranes prompted us to investigate the possibility of developing derivatives of $\mathbf{14}^{4+}$ as antimicrobials.

Our initial study, involving $\mathbf{15}^{4+}$, $\mathbf{17}^{4+}$, and two new complexes, $\mathbf{24}^{4+}$ and $\mathbf{25}^{4+}$(see Fig 17 for structures), investigated their activity against a wild-type strain of Gram-negative *Escherichia coli*, MG1655, a uropathogenic multi-drug resistant EC958 ST131 *E. coli* strain and a pathogenic strain of *Enterococcus faecalis*, *V583* (ATCC 700802); this Gram-positive bacterium is a major opportunistic pathogen and a leading cause of urinary tract infections.

It was found that whilst all the complexes had some activity against the therapeutically resistant bacteria, $\mathbf{25}^{4+}$ was particularly potent, being more bactericidal than ampicillin against the wild-type *E coli* strain, a potency that was retained in the pathogenic strain and resistant *E faecalis*.

Fascinatingly, the uptake of the ruthenium complex seems - at least in part - to be energy dependent. In glucose-free conditions, internalisation of $\mathbf{25}^{4+}$ is over two phases. After an initial post-exposure increase, intracellular ruthenium levels do not change for ~ 20 min, after which they double to a concentration above 1 mM. Yet, in the presence of glucose the uptake of the complex is rapid, with the same final intracellular concentration of ruthenium being reached within 20 min. These observations suggest that after a period of exposure to $\mathbf{25}^{4+}$ bacterial cell wall damage occurs rendering it permeable to the complex and thus allowing passive uptake of the complex. As $\mathbf{25}^{4+}$ is too large for porin-mediated uptake (which requires molecules with masses <600 Da), this mechanism can be discounted.

As $\mathbf{25}^{4+}$retains the excellent imaging capabilities of the parent complex, its mode of action was investigated using an array of microscope-based methods. Through a combination of SIM and STED experiments, it was found that, after a 20-minute induction period, bacterial internalisation of $\mathbf{25}^{4+}$ could be visualized through its characteristic emission, but before this time, the complex largely accumulates at cellular membranes and after internalization it increasingly preferentially locates at the cell poles.

Further evidence of cell membrane damage was provided by co-staining experiments. Alexa Fluor NHS-ester 405 is a cell impermeable membrane probe; but, in cells that are also exposed to $\mathbf{25}^{4+}$, NHS-ester 405 internalises. Complex-induced membrane damage was confirmed through an ATP leakage assay and TEM experiments with treated *E. coli* EC958 cells in which blebbing of the membrane, outer membrane detachment, and cell lysis were directly visualized – Fig 19A.

Despite the radical morphological effects on prokaryotes, MTT-assays on human embryonic kidney cells, HEK293, yielded an average estimated IC_{50} of 135 μM, meaning that there is an 80-fold, or larger, difference in the complex's inhibitory concentration against bacteria and non-malignant human cells. This data is consistent with a toxicity screen carried out using *Galleria mellonella.* The larvae of *Galleria* have proven to be useful *in vivo* models which have yielded data that is at least as reliable as commonly used mammalian models. *Galleria* survival, activity, and melanisation scores on exposure to a range of complex concentrations showed that there was no significant negative effects in *Galleria* treated with $\mathbf{25}^{4+}$, which confirmed that - even at concentrations well above its MIC - the complex is not toxic to a live multicell organism.[92]

The observation that $\mathbf{25}^{4+}$ is particularly potent against Gram-negative bacteria was intriguing. One of the major differences between Gram-positive and Gram-negative bacteria is, or course, the composition of their cell-wall and - as initial study demonstrated that the complex disrupted the cell-wall of a Gram-negative pathogen – we therefore set out to examine whether there were differences in its effect on Gram-positive bacteria. In these studies, we used a wild type strain of *Staphylococcus aureus* (SH1000) and several resistant, pathogenic strains including a methicillin-resistant, MRSA, variant. We chose this bacterium because, as the therapeutic resistance mechanisms of specific strains are well understood, it can be used as a test-bed to explore the action of new antimicrobials at a molecular scale.

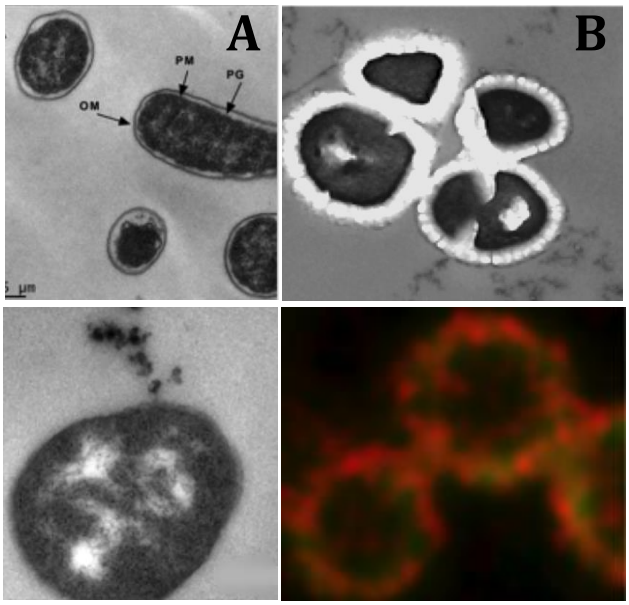

Fig. 19 Images reveal the antimicrobial Activity of $\mathbf{25}^{4+}$. A: TEM experiments showing *E. coli* EC958 cells before treatment (Top) and the morphological changes one hour after exposure (bottom). B: TEM image showing wild-type *S. aureus* cells after one-hour exposure to $\mathbf{25}^{4+}$ illustrating swelling of cell walls (Top). STED nanoscopy of cells of an *MRSA* strain stained with $\mathbf{25}^{4+}$ revealing the complex is clearly retained on/in the cell-wall in a distinctive pattern of distribution. Adapted with permission from reference 93.

It was found that $\mathbf{25}^{4+}$ displayed activity against the wild-type SH1000 strain that was comparable to our previous studies and, again, there was evidence that it could be internalised through an active transport mechanism. Furthermore, super-resolution microscopy, TEM, and other experiments confirmed that, after ~1-hour exposure to $\mathbf{25}^{4+}$ at concentrations above its MIC the complex disrupted the *S Aureus* cell-membrane (Fig 19B). After this period the complex is internalized and it binds to DNA. Although all these observations seemed very similar to those made with *E coli*, there were distinctive differences. Most notably, 3D-STED images showed that the complex produced a punctate pattern over the

entire *S. aureus* outer surface, suggesting that the initial interaction of the complex with Gram-positive and Gram-negative bacteria may be different.

One distinctive feature of Gram-positive bacteria is that their cell-walls commonly contain the glycopolymers wall teichoic acid, WTA, and lipoteichoic acid, LTA. These molecules contain anionic residues and moieties that protrude from the cell wall, which means they are capable of binding to extracellular metal cations. To investigate whether **25**$^{4+}$ binds to these cell-wall components to produce the observed punctate pattern, experiments on mutant *S. aureus* strains deficient in WTA and LTA were carried out.

An immediately striking result was the increased therapeutic potency of **25**$^{4+}$ against these strains, which provided evidence that binding to teichoic acid affects its activity. Consistent with this hypothesis, although the familiar punctate accumulation pattern did not arise when one of the WTA-depleted strains of *S. aureus* was treated with **25**$^{4+}$, brighter luminescence from the internalized complex *was* observed. Conversely, a known mechanism of resistance in MRSA strains is upregulation of WTA and LTA. When such a strain was treated with **25**$^{4+}$ corresponding STED images revealed that, although the complex did not internalize, the characteristic punctate pattern on the cell wall was distinctly more pronounced, Fig 19B, providing further evidence that electrostatic binding to WTA and LTA lowers susceptibility to the complex by inhibiting its internalization.

Related experiments with a *mprF* knockout strain of *S. aureus* also led to revealing results. This gene controls a process that increases positive charge on the outer surface of the *S. aureus* membrane, reducing its susceptibility to cationic antibiotics and = as might therefore be expected - it was found that the *mprF* knock-out was considerably more susceptible to **25**$^{4+}$ than any of the other strains employed in the study. [93]

It was concluded that the identification of these resistance within Gram-positive bacteria would facilitate the synthesis of future derivatives designed to mitigate their deleterious effects on the therapeutic action of **25**$^{4+}$.

A self-assembled sensitizer for PDT

Over the last two decades, interest in metal-directed self-assembly of macrocycles and cages has massively grown. Right from the beginning such studies focussed on the design of hosts, and sensors for a variety of molecular substrates. [94,95] Yet, it is only recently that the bioactivity of these architectures has begun to be examined. [96] In the early days of such studies, we began to investigate the potential of luminescent heterometallic structures as binding substrates for biomolecules. [97,98]

A Ru_2Re_2 macrocycle, **33**$^{4+}$, was identified as a promising lead for such work. As it had already been determined that the macrocycle was a host for simple anions in non-aqueous solvents - and its crystal structure revealed that it has a "cupped palm" structure, Fig 20A and B, [98] that has some structural resemblance to the binding site of a DNA binding transcription factor TATA box binding protein, TBP - the DNA binding properties of **33**$^{4+}$ in water was investigated.

It was found that the macrocycle recognizes duplex DNA with high affinities (>10^6 M^{-1}) and, like TBP, it induces pronounced duplex bending. Given that **33**$^{4+}$ is incapable of intercalating, it was concluded that the macrocycle must externally bind to DNA through a motif that is similar to that of TBP. [99,100] These observations prompted progression to cell-based studies.

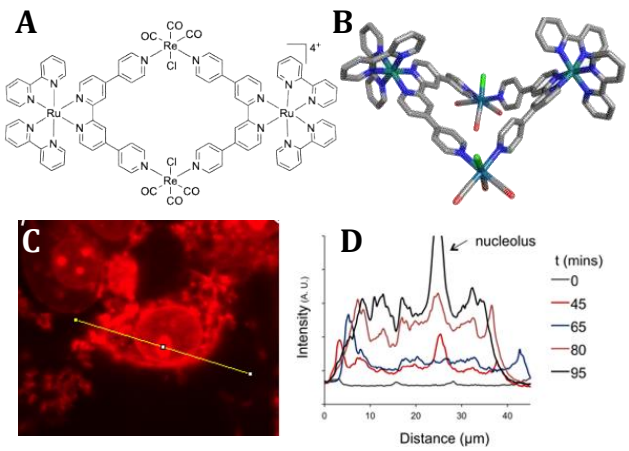

Fig 20 A Macrocycle **26**$^{4+}$ B Detail of X-ray structure of [**26**]$(PF_6)_4$ showing the structure of the **26**$^{4+}$ cation. C Swollen morphology of irradiated live MCF7 cell pre-treated with [**26**]Cl 100 minutes after exposure D Time dependent emission profile of the cell showing increase in intensity from the nucleus, particularly the nucleolus, after initial plasma membrane staining. Adapted from references 98 and 101 with permission.

Fixed MCF7 breast cancer cells treated with **26**$^{4+}$ did exhibit non-specific nuclear staining, but bright emission from lipid rich regions of the cell, such as the nuclear membrane and endoplasmic reticulum was also observed. However, equivalent treatment of live cells led to very different results. After 20 minutes exposure to the macrocycle, cells were placed in fresh, complex-free, media and any emission from **26**$^{4+}$ was monitored by CLSM. Initially, only membrane staining occurred; but, within an hour, emission from nuclei and particularly nucleoli was observed. This was then followed by slower general staining of the nuclear membrane and other membrane-enclosed structures in the cytoplasm such as endosomes, lysosomes, and the ER. This last change in emission localization was accompanied by cell swelling characteristic of oncosis. – Fig 20C and D As these effects were only observed following exposing the treated cell to light, indicating that **33**$^{4+}$ is phototoxic, the ability of the macrocycle to generate singlet oxygen on photoexcitation was investigated.

Interestingly, despite the fact that **27**$^{2+}$ - the mononuclear Ru^{II} complex used as a "building block" to construct the macrocycle - is actually a better $^1O_2$ sensitizer than **26**$^{4+}$ ($\phi(^1O_2) = 54 \pm 5$ % for the macrocycle and 75 ± 2 % for **27**$^{2+}$, respectively) it does not display the same potent phototoxicity as **27**$^{4+}$. This apparent anomaly was resolved by ICP-MS data, which showed that intracellular ruthenium concentrations were approximately seven times higher on treatment with the macrocycle as opposed to **27**$^{2+}$. Thus, the striking PDT properties of **26**$^{4+}$ are, at least in part, due to its enhanced cell uptake properties compared to the mononuclear complex. Presumably, the lower charge density of the macrocycle increases its lipophilicity compared to **27**$^{2+}$.[101]

This first report of a metal-ion templated self-assembled sensitizer offered a new paradigm for PDT because the photophysical and biophysical properties of such architectures can be optimized using relatively simple, mononuclear complex as construction modules,

Conclusions

The work outlined in this review demonstrates how bio-functional structures can be developed through the judicious selection of specific transition metal ions and ligands. As illustrated by the examples discussed herein this approach can be developed to create new optical probes, therapeutics, phototherapeutic and theranostics. Furthermore, because the synthesis of these new oligonuclear complexes is essentially modular in nature, they can be readily accessed through relatively simple synthetic methods that, if required, can provide multigram quantities. Through the judicious selection of metal and ligand components, the structure and function of these lead molecules can be easily further developed through iteration so that species with highly specific targets and function can be evolved. The inclusion of metal centres into these species provides a spectrum of imaging modalities to facilitate the identification of action mechanisms of such therapeutic leads.

Acknowledgements

The largesse of research organisations and governments in funding this research is gratefully acknowledged. Apart from the specific co-studies mentioned in this review, JAT is indebted to long-term collaborations with the groups of Julia Weinstein, Anthony Meijer, Mike Williamson and Carl Smythe at the University of Sheffield, as well as Niek Buurma (Cardiff University), and Vitor Felix (Universidade de Aveiro) whose contributions hugely improved the quality of all outputs. A number of the studies described herein were only possible through access to the Central Laser Facility, Rutherford Appleton Laboratory, which was greatly appreciated. None of this work would have been possible without the input and commitment of talented graduate, postgraduate and postdoctoral researchers.

We thank the reviewers for their insightful comments that have greatly enhanced the quality of this Feature.

Finally, JAT thanks The Royal Society for awarding him a life-changing University Research Fellowship despite his somewhat unconventional early career arc.

Notes and references

[a]*The Graduate Center, CUNY, 365 Fifth Avenue, New York, NY 10016, USA*
[b]*CRUK/MRC Oxford Institute for Radiation Oncology University of Oxford, Oxford, Oxfordshire, UK OX3 7DQ*
[c]*Department of Chemistry, University of Sheffield, Sheffield S10 2TN, U.K*
E-mail: james.thomas@sheffield.ac.uk

1 B. Rosenberg, L. Van Camp, J. E. Trosko and V. H. Mansour, *Nature*, 1969, **222**, 385–386.
2 E. Wong and C. M. Giandornenico, *Chem. Rev.*, 1999, **99**, 2451–2466.
3 L. Kelland, *Nat Rev Cancer*, 2007, **7**, 573–584.
4 D. Wang and S. J. Lippard, *Nat Rev Drug Discov*, 2005, **4**, 307–320.
5 V. Cepeda, M. A. Fuertes, J. Castilla, C. Alonso, C. Quevedo and J. M. Perez, 2007, **7**, 3–18.
6 T. Boulikas, A. Pantos, E. Bellis and P. Christofis, *Cancer Therapy*, 2007, **5**, 537–583.
7 N. J. Wheate, S. Walker, G. E. Craig and R. Oun, *Dalton Trans*, 2010, **39**, 8113–16.
8 M. G. Apps, E. H. Y. Choi and N. J. Wheate, *Endocrine Related Cancer*, 2015, **22**, R219–R233.
9 J. K. Barton, A. Danishefsky and J. Goldberg, *J. Am. Chem. Soc.*, 1984, **106**, 2172–2176.
10 C. V. Kumar, J. K. Barton and N. J. Turro, *J. Am. Chem. Soc.*, 1985, **107**, 5518–5523.
11 A. M. Pyle, J. P. Rehmann, R. Meshoyrer, C. V. Kumar, N. J. Turro and J. K. Barton, *J. Am. Chem. Soc.*, 1989, **111**, 3051–3058.
12 A. E. Friedman, J. C. Chambron, J. P. Sauvage, N. J. Turro and J. K. Barton, *J. Am. Chem. Soc.*, 1990, **112**, 4960–4962.
13 J. Olofsson, B. Önfelt and P. Lincoln, *J. Phys. Chem. A*, 2004, **108**, 4391–4398.
14 C. Hiort, P. Lincoln and B. Nordén, *J. Am. Chem. Soc.*, 1993, **115**, 3448–3454.
15 H. Niyazi, J. P. Hall, K. O'Sullivan, G. Winter, T. Sorensen, J. M. Kelly and C. J. Cardin, 2012, **4**, 621–628.
16 J. P. Hall, D. Cook, S. R. Morte, P. McIntyre, K. Buchner, H. Beer, D. J. Cardin, J. A. Brazier, G. Winter, J. M. Kelly and C. J. Cardin, *J. Am. Chem. Soc.*, 2013, **135**, 12652–12659.
17 C. J. Cardin, J. M. Kelly and S. J. Quinn, *Chem. Sci.*, 2017, **8**, 4705–4723.
18 Y. Jenkins, A. E. Friedman, N. J. Turro and J. K. Barton, *Biochemistry*, 1992, **31**, 10809–10816.
19 E. Tuite, P. Lincoln and B. Nordén, *J. Am. Chem. Soc.*, 1997, **119**, 239–240.
20 C. G. Coates, J. J. McGarvey, P. L. Callaghan, M. Coletti and J. G. Hamilton, *J. Phys. Chem. B*, 2001, **105**, 730–735.
21 S. Shi, J. Zhao, X. Geng, T. Yao, H. Huang, T. Liu, L. Zheng, Z. Li, D. Yang and L. Ji, *Dalton Trans*, 2010, **39**, 2490.
22 J. C. Chambron and J.-P. Sauvage, *Chem. Phys. Lett.*, 1991, **182**, 603–607.
23 N. P. Cook, V. Torres, D. Jain and A. A. Martí, *J. Am. Chem. Soc.*, 2011, **133**, 11121–11123.
24 N. P. Cook, K. Kilpatrick, L. Segatori and A. A. Martí, *J. Am. Chem. Soc.*, 2012, **134**, 20776–20782.
25 C. A. Puckett and J. K. Barton, *J. Am. Chem. Soc.*, 2007, **129**, 46–47.
26 C. A. Puckett and J. K. Barton, *J. Am. Chem. Soc.*, 2009, **131**, 8738–8739.
27 C. A. Puckett and J. K. Barton, *Bioorganic & Medicinal Chemistry*, 2010, **18**, 3564–3569.
28 P. Lincoln and B. Nordén, *Chem. Commun.*, 1996, 2145.
29 B. Önfelt, P. Lincoln and B. Nordén, *J. Am. Chem. Soc.*, 1999, **121**, 10846–10847.
30 F. Westerlund, M. P. Eng, M. U. Winters and P. Lincoln, *J. Phys. Chem. B*, 2007, **111**, 310–317.
31 J. Andersson and P. Lincoln, *J. Phys. Chem. B*, 2011, **115**, 14768–14775.
32 B. Önfelt, P. Lincoln and B. Nordén, *J. Am. Chem. Soc.*, 2001, **123**, 3630–3637.
33 L. M. Wilhelmsson, F. Westerlund, P. Lincoln and B. Nordén, *J. Am. Chem. Soc.*, 2002, **124**, 12092–12093.
34 P. Nordell, F. Westerlund, L. M. Wilhelmsson, B. Nordén and P. Lincoln, *Angew. Chem. Int. Ed.*, 2007, **46**, 2203–2206.
35 F. Westerlund, P. Nordell, B. Nordén and P. Lincoln, *J. Phys. Chem. B*, 2007, **111**, 9132–9137.
36 J. A. Thomas, *Chem Soc Rev*, 2015, **44**, 4494–4500.
37 E. Baggaley, J. A. Weinstein and J. A. Williams, *Coord. Chem. Rev.*, 2012, **256**, 1762–1785.
38 K. Qiu, Y. Chen, T. W. Rees, L. Ji and H. Chao, *Coord Chem Rev*, 2019, **378**, 66–86.
39 K. E. Erkkila, D. T. Odom and J. K. Barton, *Chem. Rev.*, 1999, **99**, 2777–2796.
40 A. C. Komor and J. K. Barton, *Chem. Commun.*, 2013, **49**, 3617–3630.
41 H. D. Stoeffler, N. B. Thornton, S. L. Temkin and K. S. Schanze, *J. Am. Chem. Soc.*, 1995, **117**, 7119–7128.
42 V. Yam, K. Lo, K. K. Cheung and R. Kong, *J. Chem. Soc., Chem. Commun.*, 1995, **0**, 1191–1193.
43 V. W.-W. Yam, K. K.-W. Lo, K.-K. Cheung and R. Y.-C. Kong, *J. Chem. Soc., Dalton Trans.*, 1997, 2067–2072.
44 A. Llobet, P. Doppelt and T. J. Meyer, *Inorg Chem*, 1988, **27**, 514–520.

45 C. Metcalfe, H. Adams, I. Haq and J. A. Thomas, *Chem. Commun.*, 2003, 1152–1153.
46 I. Haq, P. Lincoln, D. Suh, B. Nordén, B. Z. Chowdhry and J. B. Chaires, *J. Am. Chem. Soc.*, 1995, **117**, 4788–4796.
47 C. Metcalfe, M. Webb and J. A. Thomas, *Chem. Commun.*, 2002, 2026–2027.
48 C. Metcalfe, I. Haq and J. A. Thomas, *Inorg Chem*, 2004, **43**, 317–323.
49 S. P. Foxon, T. Phillips, M. R. Gill, M. Towrie, A. W. Parker, M. Webb and J. A. Thomas, *Angew. Chem. Int. Ed.*, 2007, **46**, 3686–3688.
50 J. B. Chaires, F. Leng, T. Przewloka, I. Fokt, Y.-H. Ling, R. Perez-Soler and W. Priebe, *J. Med. Chem.*, 1997, **40**, 261–266.
51 P. Waywell, V. Gonzalez, M. R. Gill, H. Adams, A. J. H. M. Meijer, M. P. Williamson and J. A. Thomas, *Chem. Eur. J.*, 2010, **16**, 2407–2417.
52 M. G. Walker, V. Gonzalez, E. Chekmeneva and J. A. Thomas, *Angew. Chem. Int. Ed.*, 2012, **51**, 12107–12110.
53 H. K. Saeed, I. Q. Saeed, N. J. Buurma and J. A. Thomas, *Chem. Eur. J.*, 2017, **23**, 5467–5477.
54 R. M. Hartshorn and J. K. Barton, *J. Am. Chem. Soc.*, 1992, **114**, 5919–5925.
55 S. P. Foxon, M. A. H. Alamiry, M. G. Walker, A. J. H. M. Meijer, I. V. Sazanovich, J. A. Weinstein and J. A. Thomas, *J. Phys. Chem. A*, 2009, **113**, 12754–12762.
56 Y. Sun, L. E. Joyce, N. M. Dickson and C. Turro, *Chem. Commun.*, 2010, **46**, 2426.
57 Hiwa K. Saeed, Paul J. Jarman, Stuart Archer, Sreejesh Sreedharan, Ibrahim Q. Saeed, Luke K. Mckenzie, Julia A. Weinstein, Niklaas J. Buurma, Carl G. W. Smythe, and Jim A. Thomas, *Angew. Chem. Int. Ed.*, 2017, **56**, 12628–12633.
58 M. Gellert, M. N. Lipsett and D. R. Davies, *Proc Natl Acad Sci USA*, 1962, **48**, 2013–&.
59 J. T. Davis, *Angew. Chem. Int. Ed.*, 2004, **43**, 668–698.
60 J. L. Huppert, *Chem Soc Rev*, 2008, **37**, 1375.
61 P. Murat and S. Balasubramanian, *Curr. Opin. Genet. Dev.*, 2014, **25**, 22–29.
62 S. Neidle, *Nat. Rev. Chem.*, 2017, **1**, 0041.
63 J. Bolger, A. Gourdon, E. Ishow and J.-P. Launay, *Inorg Chem*, 1996, **35**, 2937–2944.
64 C. Rajput, R. Rutkaite, L. Swanson, I. Haq and J. A. Thomas, *Chem. Eur. J.*, 2006, **12**, 4611–4619.
65 T. Wilson, M. P. Williamson and J. A. Thomas, *Org. Biomol. Chem.*, 2010, **8**, 2617–2621.
66 D. A. Lutterman, A. Chouai, Y. Liu, Y. Sun, C. D. Stewart, K. R. Dunbar and C. Turro, *J. Am. Chem. Soc.*, 2008, **130**, 1163–1170.
67 S. D. Fairbanks, C. C. Robertson, F. R. Keene, J. A. Thomas and M. P. Williamson, *J. Am. Chem. Soc.*, 2019, **141**, 4644–4652.
68 T. Wilson, P. J. Costa, V. Félix, M. P. Williamson and J. A. Thomas, *J. Med. Chem.*, 2013, **56**, 8674–8683.
69 M. R. Gill, J. Garcia-Lara, S. J. Foster, C. Smythe, G. Battaglia and J. A. Thomas, *Nat Chem*, 2009, **1**, 662–667.
70 A. Wragg, M. R. Gill, C. J. Hill, X. Su, A. J. H. M. Meijer, C. Smythe and J. A. Thomas, *Chem. Commun.*, 2014, **50**, 14494–14497.
71 M. R. Gill, D. Cecchin, M. G. Walker, R. S. Mulla, G. Battaglia, C. Smythe and J. A. Thomas, *Chem. Sci.*, 2013, **4**, 4512–4519.
72 Ł. Skórka, M. Filapek, L. Zur, J. G. Małecki, W. Pisarski, M. Olejnik, W. Danikiewicz and S. Krompiec, *J. Phys. Chem. C*, 2016, **120**, 7284–7294.
73 A. Wragg, M. R. Gill, D. Turton, H. Adams, T. M. Roseveare, C. Smythe, X. Su and J. A. Thomas, *Chem. Eur. J.*, 2014, **20**, 14004–14011.
74 A. Wragg, M. R. Gill, L. McKenzie, C. Glover, R. Mowll, J. A. Weinstein, X. Su, C. Smythe and J. A. Thomas, *Chem. Eur. J.*, 2015, **21**, 11865–11871.
75 E. Baggaley, M. R. Gill, N. H. Green, D. Turton, I. V. Sazanovich, S. W. Botchway, C. Smythe, J. W. Haycock, J. A. Weinstein and J. A. Thomas, *Angew. Chem. Int. Ed.*, 2014, **53**, 3367–3371.
76 H. Blom and J. Widengren, *Chem. Rev.*, 2017, **117**, 7377–7427.
77 S. Sreedharan, M. R. Gill, E. Garcia, H. K. Saeed, D. Robinson, A. Byrne, A. Cadby, T. E. Keyes, C. Smythe, P. Pellett, J. Bernardino de la Serna and J. A. Thomas, *J. Am. Chem. Soc.*, 2017, **139**, 15907–15913.
78 S. A. Tysoe, R. Kopelman and D. Schelzig, *Inorg Chem*, 1999, **38**, 5196–5197.
79 M. R. Gill, H. Derrat, C. G. W. Smythe, G. Battaglia and J. A. Thomas, *Chembiochem*, 2011, **12**, 877–880.
80 P. J. Jarman, F. Noakes, S. Fairbanks, K. Smitten, I. K. Griffiths, H. K. Saeed, J. A. Thomas and C. Smythe, *J. Am. Chem. Soc.*, 2018, **141**, 2925–2937.
81 M. R. Gill, P. J. Jarman, S. Halder, M. G. Walker, H. K. Saeed, J. A. Thomas, C. Smythe, K. Ramadan and K. A. Vallis, *Chem. Sci.*, 2018, **9**, 841–849.
82 M. R. Gill, J. U. Menon, P. J. Jarman, J. Owen, I. Skaripa-Koukelli, S. Able, J. A. Thomas, R. Carlisle and K. A. Vallis, *Nanoscale*, 2018, **10**, 10596–10608.
83 J. Ghesquière, S. Le Gac, L. Marcélis, C. Moucheron and A. K.-D. Mesmaeker, *Curr Top Med Chem*, 2012, **12**, 185–196.
84 I. I. Ortmans, B. B. Elias, J. M. J. Kelly, C. C. Moucheron and A. A. Kirsch-DeMesmaeker, *Dalton Trans*, 2004, 668–676.
85 J. P. Hall, F. E. Poynton, P. M. Keane, S. P. Gurung, J. A. Brazier, D. J. Cardin, G. Winter, T. Gunnlaugsson, I. V. Sazanovich, M. Towrie, C. J. Cardin, J. M. Kelly and S. J. Quinn, *Nat Chem*, 2015, **7**, 961–967.
86 S. M. Cloonan, R. B. P. Elmes, M. Erby, S. A. Bright, F. E. Poynton, D. E. Nolan, S. J. Quinn, T. Gunnlaugsson and D. C. Williams, *J. Med. Chem.*, 2015, **58**, 4494–4505.
87 S. A. Archer, A. Raza, F. Dröge, C. Robertson, A. J. Auty, D. Chekulaev, J. A. Weinstein, T. Keane, A. J. H. M. Meijer, J. W. Haycock, S. MacNeil and J. A. Thomas, *Chem. Sci.*, 2019, **10**, 3502–3513.
88 E. Toner, A. Adalja, G. K. Gronvall, A. Cicero and T. V. Inglesby, *Health Security*, 2015, **13**, 153–155.
89 Z.-Q. Xu, M. T. Flavin and J. Flavin, *Expert Opin. Investig. Drugs*, 2014, **23**, 000–000.
90 F. P. Dwyer, E. C. Gyarfas, W. P. Rogers and J. H. Koch, *Nature*, 1952, **170**, 190–191.
91 F. Li, J. G. Collins and F. R. Keene, *Chem Soc Rev*, 2015, **44**, 2529–2542.
92 K. L. Smitten, H. M. Southam, J. Bernardino de la Serna, M. R. Gill, P. J. Jarman, C. G. W. Smythe, R. K. Poole and J. A. Thomas, *ACS Nano*, 2019, **13**, 5133–5146.
93 K. L. Smitten, S. D. Fairbanks, C. C. Robertson, J. Bernardino de la Serna, S. J. Foster and J. A. Thomas, *Chem. Sci.*, 2020, **11**, 70-79.
94 J. A. Thomas, *Dalton Trans*, 2011, **40**, 12005–12016.
95 T. R. Cook and P. J. Stang, *Chem. Rev.*, 2015, **115**, 7001–7045.
96 T. R. Cook, V. Vajpayee, M. H. Lee, P. J. Stang and K.-W. Chi, *Acc. Chem. Res.*, 2013, **46**, 2464–2474.
97 P. de Wolf, S. L. Heath and J. A. Thomas, *Chem. Commun.*, 2002, 2540–2541.
98 P. de Wolf, P. Waywell, M. Hanson, S. L. Heath, A. J. H. M. Meijer, S. J. Teat and J. A. Thomas, *Chem. Eur. J.*, 2006, **12**, 2188–2195.
99 D. Ghosh, H. Ahmad and J. Thomas, *Chem. Commun.*, 2009, 2947–2949.
100 H. Ahmad, D. Ghosh and J. A. Thomas, *Chem. Commun.*, 2014, **50**, 3859–3861.
101 M. G. Walker, P. J. Jarman, M. R. Gill, X. Tian, H. Ahmad, P. A. N. Reddy, L. McKenzie, J. A. Weinstein, A. J. H. M. Meijer, G. Battaglia, C. G. W. Smythe and J. A. Thomas, *Chem. Eur. J.*, 2016, **22**, 5996–6000.